1 **Influence of crustal mechanical layering on the seismic potential of active**
2 **faults: insights from the southwestern Valencia Trough (W Mediterranean)**

4 Martin-Rojas, Iván[1]

5 Ramos, Adriá[1]

6 De Ruig, Menno[2]

7 Medina-Cascales, Iván[1]

8 Santamaría-Pérez, Eva[1]

9 Alfaro, Pedro[1]

11 1 Dpto. de Ciencias de la Tierra y del Medio Ambiente, Universidad de Alicante,
12 Campus San Vicente s/n, 03690, San Vicente del Raspeig, Alicante.
13 ivan.martin@ua.es

14 2. Oropesa BV, Van Bleiswijkstraat 183, 2582 LD The Hague, Netherlands.
15 menno.deruig@gmail.com

17 Corresponding author: Martin-Rojas, Iván

18 Dpto. de Ciencias de la Tierra y del Medio Ambiente, Universidad de Alicante,
19 Campus San Vicente s/n, 03690, San Vicente del Raspeig, Alicante.
20 ivan.martin@ua.es

23   **Short summary**

24   This study investigates the main active faults located within the southwestern

25   Valencia Trough, an offshore region east of the Spanish coast. Utilizing subsurface

26   data, we identify and characterize the 3D geometry of several of these faults for the

27   first time. Given that active faults pose a significant natural hazard due to their

28   potential to generate earthquakes, we also assess the seismic potential of the faults

29   within the southwestern Valencia Trough.

ABSTRACT

We present a structural and seismotectonic analysis of active faults in the southwestern Valencia Trough (western Mediterranean) on the basis of subsurface datasets. In our study, we identify and characterise three major active faults: the Cullera Fault, with a long-term slip rates that vary over time between 0.15 ± 0.1 mm/yr and 0.4 ± 0.1 mm/yr; the oblique Albufera Fault, with a long-term slip rate of 0.2 ± 0.1 mm/yr; and the normal Valencia Fault.

The seismogenic character of the southwestern Valencia Trough is controlled by a mechanically weak layer consisting of Triassic evaporites. This weak layer induces partial to complete decoupling between the suprasalt and subsalt successions, leading to two distinct mechanisms driving fault displacement: tectonic activity and salt withdrawal. A quantitative evolutionary analysis of the Cullera Fault reveals that these two mechanisms alternate over time.

The presence of a mechanically weak layer has implications for seismicity. Earthquakes can nucleate within both sub- and suprasalt successions, with total or partial decoupling influencing rupture propagation. We discuss how these two scenarios lead to different earthquakes and thus impact the seismic hazard of a region. Empirical source-scaling relationships, which are commonly used to estimate the seismogenic potential of active faults, generally assume a homogeneous seismogenic crust. To address this limitation, we propose a methodological approach based on the use of the aspect ratio. Our findings highlight the need to incorporate stratigraphic mechanical layering into seismic hazard assessments, particularly in salt-influenced tectonic settings.

1. Introduction

Seismic-hazard analyses are often performed by scaling relationships. These relationships are regressions in which the seismogenic potential of active faults is derived from geometric parameters of the fault, such as the potential fault rupture length or area (Stirling et al., 2013). Pioneering works on scaling relationships began in the 1970s (Kanamori & Anderson, 1975; Geller, 1976). The regressions of Wells & Coppersmith (1994) represent a milestone in the application of scaling relationships, as they included a very large dataset of historical earthquakes. The equations proposed by Wells & Coppersmith became a standard for determining the seismogenic potential of active faults. Subsequently, other scaling relationships have been proposed, accounting for factors such as the tectonic environment, fault dip, or seismogenic thickness (Stirling et al., 2002 and 2013; Leonard 2010 and 2014; Huang et al., 2024, among many others).

Most scaling relationships employed to evaluate crustal earthquakes correlate the moment magnitude (Mw) with the fault dimensions (length, width, and/or area). Some of these scaling relationships consider the fault width vs. fault dip growth of ruptures for large earthquakes, as rupture width is limited by the maximum depth of the seismogenic crust (Leonard, 2010; Yen and Ma, 2011; Leonard, 2014; Cheng et al., 2019). However, these relationships do not consider the influence of potential heterogeneities within the seismogenic crust, which could control the propagation of ruptures and, therefore, the magnitude of earthquakes.

Here, we present an analysis of several subsurface datasets, including high-resolution seismic profiles, from the southwestern Valencia Trough. We identify and characterise the main active faults in this region, and we carry out a detailed geometric description. The results of this analysis also emphasize that this region is characterised by a mechanically weak layer within the seismogenic crust. After mapping the main faults, we apply conventional scaling relationships to evaluate the potential magnitudes of future earthquakes. We propose a methodological approach for integrating the effects of mechanically weak layers—such as Triassic evaporites—into routine seismic hazard assessments, highlighting the need to refine existing scaling relationships in tectonically complex settings.

2. Tectonic setting

The Valencia Trough is an extensional basin located in the western Mediterranean region (Fig. 1). This basin is the result of polyphase tectonic evolution spanning from the Triassic to the present day, as it is located between the Betic-Balearic fold-and-thrust belt to the south, the Iberian Chain to the west, and the Catalan Coastal Ranges to the north (De Ruig, 1992; Guimerà & Álvaro, 1990; Maillard & Mauffret, 1999; Roca & Desegaulx, 1992; Roca et al., 2004; Vergés & Fernàndez, 2012). The tectonic evolution of the Valencia Trough is also partially influenced by extension related to the retreat of the Maghrebian–Ligurian Tethys subduction slab (Etheve et al., 2016; Faccenna et al., 2004; Jolivet & Faccenna, 2000; Maillard & Mauffret, 1999; Rehault et al., 1984; Roca et al., 1999; Séranne, 1999; van Hinsbergen et al., 2014).

The Valencia Trough (Fig. 1) underwent a Mesozoic rifting process related to the Iberian intraplate rift and the opening of the Western Tethys (Arche and López-Gómez, 1996; Nebot and Guimerà, 2018; Ramos et al., 2023; Salas et al., 2001). This process led to the formation of NW–SE and NE–SW high-angle faults offsetting the pre-Mesozoic basement and to the deposition of a 5–15-km-thick Upper Jurassic–Lower Cretaceous succession.

During the Late Cretaceous, the onset of convergence between Nubia and Eurasia caused the transition from a Mesozoic extensional tectonic regime to successive compressional and extensional stages (Roca, 2001; Salas et al., 2001; Vergés and Sàbat, 1999). From the late Eocene to the Oligocene, the Valencia Trough was dominated by shortening. Onshore, this episode led to the formation of the intraplate Iberian Chain and Catalan Coastal Ranges (Gaspar-Escribano et al., 2004; Geel, 1995; Guimerà and Álvaro, 1990).

From the late Oligocene to the middle Miocene, the western Mediterranean region was subsequently affected by an extensional regime, driven by the complex interplay between the European–Cenozoic rift system (e.g., Séranne, 1999) and the rollback of the Maghrebian–Ligurian Tethys slab (Faccenna et al., 2004; van Hinsbergen et al., 2014). This extensional phase led to the formation of the Liguro-Provençal and Algerian Basins, as well as the Valencia Trough. However, subsidence in the southwestern Valencia Trough during this period cannot be accounted for by

119 rifting, due to the limited occurrence of Cenozoic basement extensional faults

120 (Roca and Guimerà, 1992). Therefore, extension has been interpreted as due to the

121 collapse of a back-arc transient uplift event (Fang et al., 2021).

122 The extension in the Valencia Trough occurred immediately before or synchronously

123 with the formation of the compressional Betic Cordillera. This compressional

124 deformation is well expressed by a thin-skinned fold-and-thrust system observed in

125 the Eastern Betic Cordillera (De Ruig, 1995; Sàbat et al., 2011) and in the Balearic

126 Promontory (Mallorca and Ibiza Islands). At the same time, significant magmatic

127 activity took place in the area, and was divided into two phases: (1) late Oligocene

128 to Serravallian calc-alkaline activity and (2) Tortonian to present alkaline volcanic

129 activity (Martí et al., 1992).

130 From the Pliocene to the present, the tectonic setting in the Valencia Trough has

131 been dominated by NE–SW extension, as indicated by focal mechanisms (Stich et

132 al., 2010) and broad regional global navigation satellite system (GNSS) analyses

133 (Stich et al., 2006). This extension has been related to thermal subsidence (Roca,

134 1992, 1996, and 2001; Roca and Guimerà, 1992; Roca et al., 1999a; Gaspar-

135 Escribano et al., 2004) and has been interpreted as the final stage of an aborted rift

136 event responsible for the ENE motion of the Balearic promontory (Palano et al.,

137 2015). Several normal active faults have been defined in the southwestern Valencia

138 Trough thus far (Fig. 1): the Western Cabo Cullera Fault, Central–Western Cabo

139 Cullera Fault, Central–Eastern Cabo Cullera Fault, Eastern Cabo Cullera Fault and

140 Southwest Columbretes Fault (Perea, 2006). Some of these faults were previously

141 recognised from vintage seismic lines (Diaz del Rio et al., 1986; Roca, 1992, 1996;

142 Perea, 2006; Maillard & Mauffret, 2013), but fault traces and geometry were defined

143 only very approximately. Similarly, the slip rates derived from the displacement of

144 Plio-Quaternary seismic reflectors observed in the vintage seismic lines present

145 high uncertainties (0.02 ±0.01 mm/yr; Perea, 2006). In the Valencia Trough,

146 seismicity is characterised by low- to moderate-magnitude events (Fig. 1). The few

147 available focal mechanisms (Stich et al., 2010; IGN, 2025) indicate a normal–

148 oblique or strike slip kinematics, although these focal mechanisms present high

149 uncertainties, mainly because they occur at long distances from seismic stations

150   and are registered with significant azimuthal gaps (González, 2017). According to

151   the data published by the Spanish Earthquake Catalogue (IGN, 2025), this

152   seismicity is very shallow, as most of the events are assigned depths of less than 10

153   km (Fig. 2). However, once again, these data should be taken with caution, as the

154   depths assigned to these earthquakes present high uncertainties (González, 2017).

155   In the onshore domain located west of the Valencia Trough, only one major active

156   structure, namely, the Jumilla Fault, has been postulated (García-Mayordomo et al.,

157   2012), together with other minor active faults (Alcoy, Mariola, and Benasau Faults).

158   In this onshore area, several significant historical earthquakes have occurred, such

159   as the 1396 Tavernes (I_{EMS98}=VIII-IX), 1620 Alcoy (I_{EMS98}=VIII-IX), 1644 Muro (I_{EMS98}=V)

160   and 1748 Estubeny (I_{EMS98}=IX) earthquakes (Martínez Solares and Mezcua, 2002;

161   IGN, 2025; Buforn et al., 2105; Buforn & Udías, 2022).
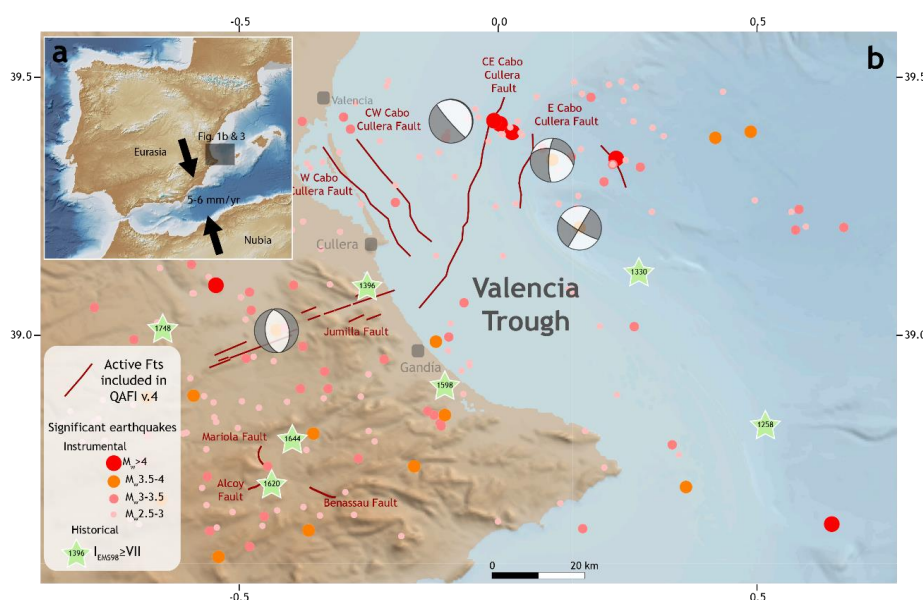
162

163   Fig. 1. a. Location of the Valencia Trough. Convergence vectors between Nubia and

164   Eurasia are after DeMets et al., 1994; McClusky et al., 2003; Nocquet, 2012;

165   Nocquet & Calais, 2003; Pérez-Peña et al., 2010; Serpelloni et al., 2007; Stich et al.,

166   2006. b. Seismotectonic map of the southwestern Valencia Trough and surrounding

167   areas. Fault traces from Quaternary-Active Faults of Iberia database (García-

168   Mayordomo et al., 2012)

169

170
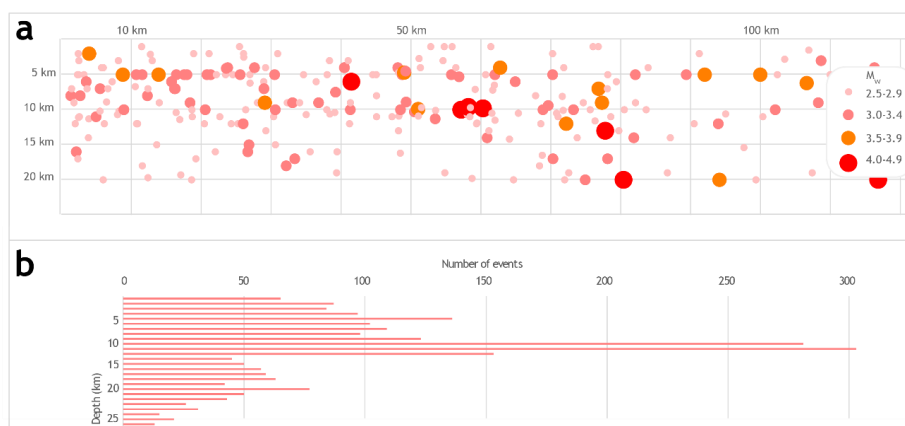
Fig 2. Seismicity of Mw>2.5 in the southwestern Valencia Trough shallower than 20 km since 1950 from the Instituto Geográfico Nacional database (IGN, 2025) a. Distribution of the depth of seismicity. Horizontal axis represents distance along the southwestern Valencia Torugh in a SW-NE direction. b. Depth histogram.

175 **3. Methods**

176 The interpretation of the offshore area is based on mainly 2D multichannel seismic

177 reflection data calibrated with well data (Fig. 3). The central part of the study area is

178 covered by a high-quality seismic survey acquired by Fugro-Geoteam with the RV

179 Geo Baltic, processed by Robertson Research International Ltd. in 2002. The survey

180 consists of 30 seismic sections with an average length of 90 km (totalling

181 approximately 2,800 km). They are oriented WNW–ESE and NNE–SSW, with

182 maximum spacings of 13 km and 6 km, respectively. The details regarding the

183 acquisition and processing parameters can be found in Cameselle & Urgeles (2017).

184 Most of the area affected by Plio-Quaternary faulting nearer to the coast is covered

185 only by vintage 2D seismic lines from the late 1970s, acquired by various operators,

186 which are publicly available upon request in the Instituto Geológico y Minero de

187 España (IGME-CSIC) (http://info.igme.es/sigeof/). More than 100 of these seismic

188 lines, with a total line length of approximately 2,500 km, were selected for mapping;

189 although the quality of these lines varies from moderate to poor, the high-density

190 grid spacing (varying from 1 to 3.5 km) allows fault mapping with reasonable

191 confidence. The seismic interpretation was performed in two-way travel time (TWT)

192 by using Move software (by Petex). The seismic dataset was converted to depths

193 using velocity data derived from Expanded Spread Profile ESP 7 (Pascal et al., 1992;

194 Torné et al., 1992). A second-order polynomial trend was applied to establish time–

195 depth relationships, ensuring strong correlation with the well data, similar to the

196 methodologies of Fang et al. (2021).

197 The interpretation of seismic horizons is calibrated by 9 offshore petroleum

198 exploration wells, all of which penetrate the entire Neogene section and whose

199 bottoms are in Mesozoic rocks. Original well reports, log data (lithology, dipmeter,

200 gamma–ray, sonic and resistivity data) and palaeontological data (from cuttings and

201 sidewall cores) were retrieved from the IGME-CSIC archive

202 (https://info.igme.es/hidrocarburos/). Well-to-seismic ties were established by

203 integrating the sonic logs and using synthetic seismograms from end-of-well

204 reports. Palaeontological analyses and range charts from the original well reports

205 were reviewed and adapted to the Mediterranean biozonation of Lirer et al. (2019) to

206 obtain approximate absolute ages for the seismic horizons.

207 No seismic data were available for the onshore area of southern Valencia and only

208 two deep exploration wells were drilled (Jaraco-1 and Perenchiza-1). However,

209 stratigraphic information is available from 95 hydrogeological wells in the Valencia

210 coastal plain, as are vertical electric sounding (VES) profiles acquired for

211 hydrogeological surveys. The data are publicly available in the online IGME-CSIC

212 databases IRYDA, BD Puntos Agua 2.0 and Sistema de Información Documental

213 (SID) (accessible through https://info.igme.es/catalogo/).

214 In areas with poor seismic coverage, structural mapping was aided by regional

215 Bouguer gravity anomalies processed with a Butterworth High-pass filter with a 1-

216 degree cut-off frequency to highlight short-wavelength features of the data (by

217 Getech, 2015).
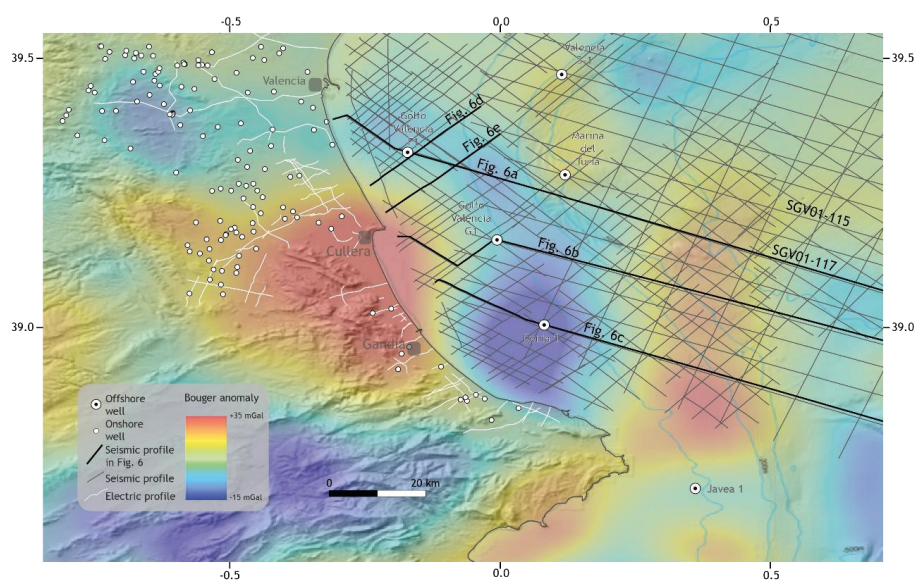
218

219 Fig. 3. Geophysical dataset used in this work. Filtered Bouguer anomaly data after

220 Getech (2015). The location is shown in figure 1.

221

4. Stratigraphy

The general stratigraphic arrangement of the southwestern Valencia Trough (Fig. 4) consists of a rigid Palaeozoic–Middle Triassic basement overlain by a 1.5–7-km Upper Triassic–Quaternary stratigraphic cover. Here we present a new detailed stratigraphic framework for the late Miocene–Quaternary of the southern Valencia Trough. The definition of the pre-Neogene stratigraphic units presented in this work is based on mainly previous literature and our analysis of well data, as well as outcrops in the mainland for the most recent sediments.

The Upper Triassic succession (Fig. 4) consists of evaporites, shales and dolomites (Keuper Facies) (Vargas et al., 2009). The Upper Triassic deposits are overlain by shallow-water dolomites and anhydrites deposited from the Early to Middle Jurassic (Salas et al., 2001). The Upper Jurassic and Lower Cretaceous successions are represented by platform carbonates that grade to marls basinwards and are overlain by middle–late Albian to Late Cretaceous carbonates. The top of the Mesozoic succession corresponds to an erosive, angular unconformity that is directly overlain by Neogene deposits. Cenozoic infilling has been broadly studied in recent decades (e.g., Arche et al., 2010; Clavell and Berástegui, 1991; Maillard et al., 1992; Ribó et al., 2016b, 2016a; Soler et al., 1983). The succession starts with a transition from continental clastic sediments to marine platform carbonates, ending with a deposit formed by progradational terrigenous shelf-talus sediments (Clavell and Berástegui, 1991; Etheve et al., 2018; Lanaja, 1987; Roca and Desegaulx, 1992; Soler et al., 1986).

The Neogene succession onshore of the southwestern Valencia Trough (Fig. 4) mostly consists of middle–late Miocene continental to marginal marine deposits. In the offshore part of the study area, the Miocene stratigraphic succession is entirely marine. The base of the Miocene sequence is composed of a basal conglomerate overlain by coralline algal limestones. The middle Miocene (late Langhian–Serravallian) deep marine calcareous claystones, marls and fine-grained sandstones overlie the algal limestones or rest directly on deeply eroded Mesozoic rocks. Within the southern and central parts of the study area, the early–middle Miocene sequence is no more than 200 m thick. Towards the north, the middle

253   Miocene interval rapidly thickens, reaching almost 2000 m. Tortonian and Messinian

254   deposits consist of mainly marls with thicknesses varying between 180 m and 425

255   m. The top of the Tortonian–Messinian series is an erosional unconformity

256   (Messinian Erosion Surface (MES)) (Stampfli & Höcker, 1989; Lofi et al., 2011;

257   Cameselle et al., 2014).

258   In the onshore and nearshore areas, upper Miocene deposits are overlain by thin

259   cover (generally less than 50 m) of Pleistocene–recent alluvial fans, laterally grading

260   to lagoonal and beach barrier deposits near the coast. No Pliocene sediments have

261   been identified in the entire onshore coastal area, except for local karstic cave infills

262   with mammal remains (Agustí et al., 2011). Below the southern parts of the city of

263   Valencia, the thickness of Pleistocene–recent deposits abruptly increases. Vertical

264   electric sounding profiles seem to indicate the presence of several large normal

265   faults in this area, which have locally dropped the top Miocene surface down to

266   more than 400 m below sea level. From Cullera southwards, shallow boreholes

267   encounter Pleistocene to recent interbedded alluvial gravels, brackish lagoon, and

268   beach barrier deposits. Vertical electric sounding profiles and well correlations

269   indicate abrupt thickness changes, likely controlled by a complex system of normal

270   faults in the Mesozoic–middle Miocene basement, ranging from less than 50 m in

271   offset to more than 200 m towards the coast. Subsidence in the southern Valencian

272   coastal area continues to the present day, as evidenced by well-documented

273   submerged beach barriers of Tyrrhenian age (Eemian interglacial, 127–106ky),

274   which are currently found between 10 and 40 m below sea level in shallow offshore

275   areas (Zazo et al, 1979; Alcántara-Carrió et al, 2012).

276   In the offshore area, Pliocene–recent sediments form a large prograding shelf

277   complex with prominent clinoforms visible in seismic data, which downlap onto the

278   MES. Prominent undulations on slope foresets are visible on most seismic lines and

279   are interpreted as sediment waves (Ribó et al., 2015). In the offshore wells, the

280   stratigraphic succession consists of an overall shallowing-upward series of thick

281   grey claystones with calcareous interbeds at the base, grading upwards into

282   sandstones and shell beds at the top. No unconformities have been identified in the

283   entire sequence, except for erosional gullies and canyons at the shelf edge. The Plio-

284   Quaternary sequence reaches a maximum thickness of approximately 3000 m.

285   To determine the Plio-Quaternary depositional history and slip rate of major faults,

286   six seismic horizons have been mapped and dated with palaeontological data from

287   offshore wells, via the biostratigraphic scheme of Lirer et al. (2019). Starting from

288   the Messinian unconformity at 5.3 Ma, seismic markers have been dated at 3.8 Ma

289   (LO of *G. margaritae*), 3.3 Ma (FO *G. bononiensis*), 2.6 Ma (LCO *G. obliquus*) and 2.0

290   Ma (FO *G. truncatulinoides*). As no samples were collected from any of the offshore

291   wells above the lower-middle Pleistocene interval, an additional marker

292   (approximately 1.0 Ma) has been picked halfway through the 2.0 Ma marker and

293   seabed (0 Ma), assuming a constant sedimentation rate.

294   Isopach maps (Fig. 5) were produced for the intervals of Pliocene (MES to 2.6 Ma

295   marker) and Pleistocene–recent (2.6 Ma marker to the seabed), revealing a

296   significant shift in the location of the depocenter. The Pliocene depocentre is

297   located very close to the southern coast near Denia, attaining a maximum thickness

298   of approximately 1500 m, whereas the Pleistocene depocentre has prograded ca.

299   20 km to the NNW, reaching a thickness of more than 1750 m. The western

300   shoreward edge of both the Pliocene and Pleistocene depocentres is controlled by

301   very large NNW–SSE-trending normal faults (see below).

302   The described stratigraphic architecture indicates significant mechanical layering

303   in the southwestern Valencia Trough. A rigid basement is overlain by a mechanically

304   weak layer represented by the Upper Triassic Keuper Facies. Above this interval, a

305   rigid Mesozoic carbonate succession is present, followed by a semirigid layer

306   composed of primarily detrital deposits.

307
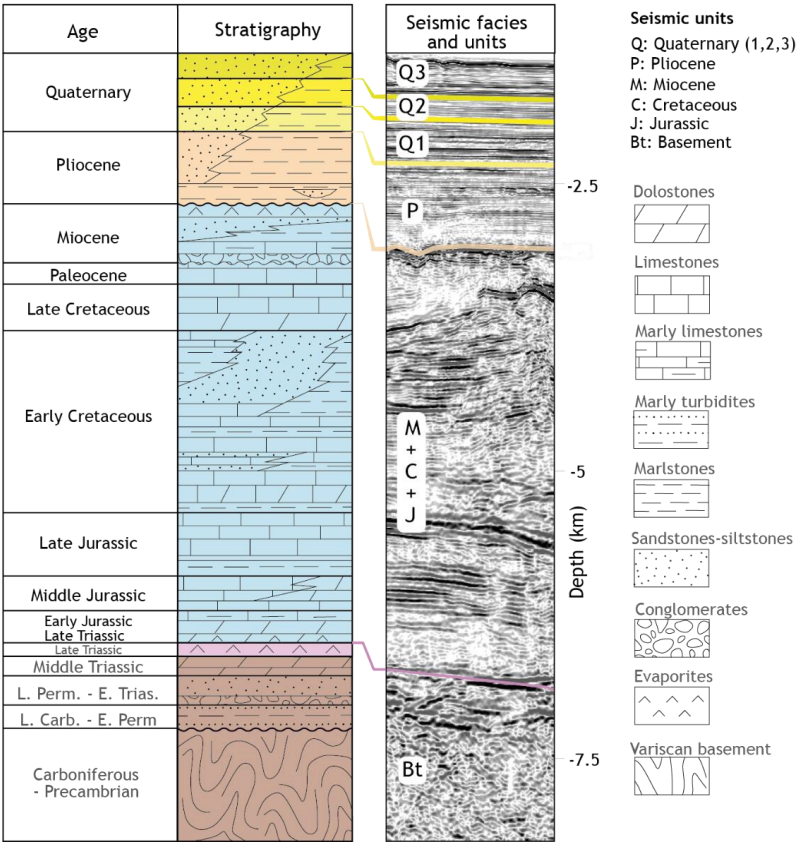
308 Figure 4: Chronostratigraphic diagram of the southwestern Valencia Trough.

309 Note that the depth scale shows maximum thicknesses ofunits.

310
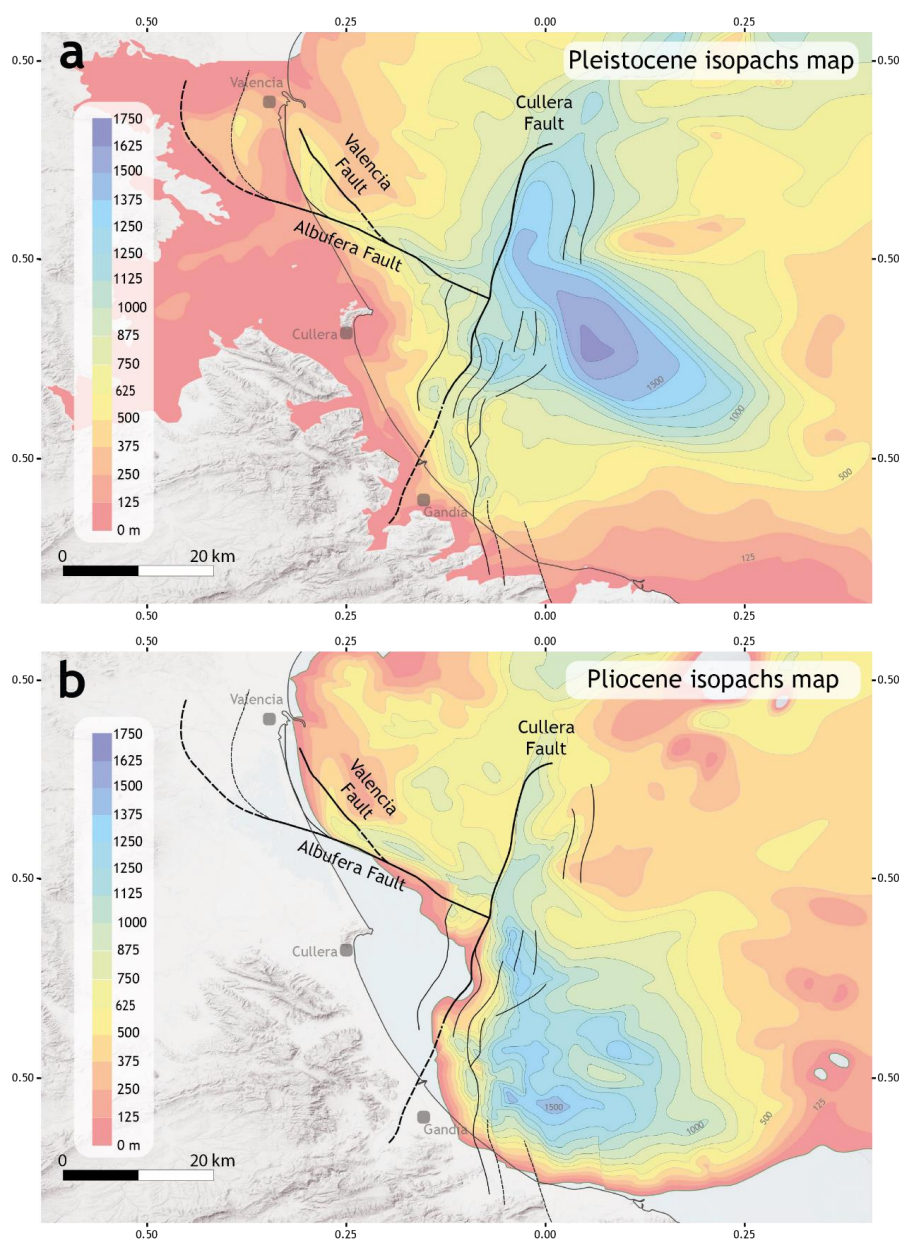
Figure 5. Isopach maps of the southwestern Valencia Trough for the Pleistocene (a) and Pliocene (b). The traces of the active faults are also depicted. Fault traces represent the horizontal projection of the direction line of the fault plane, located midway between the intersection line of the top-of-the-Pliocene horizon and the

316   top-of-the-Quaternary horizon. Fault traces are derived primarily from their position

317   on seismic profiles, supplemented by isopach maps and observed thickness

318   variations in stratigraphic units, as indicated by the available wells. Dashed lines

319   show interpreted traces. Modified from Ramos et al. (2025).

5. Main active faults in the southwestern Valencia Trough

In this section, we describe the main structural features of the southwestern Valencia Trough after the analysis of gravity data and isopach maps obtained from the subsurface dataset (seismic lines, wells and VES) (Figs. 3 and 5).

The filtered Bouguer anomaly map (Fig. 3) reveals a positive anomaly in the central part of the study area, referred to as the Cullera anomaly. This positive anomaly is surrounded by a region exhibiting a negative anomaly, particularly in the offshore area located east of Cullera. We interpret this pattern of anomaly to be because of mass excess associated with a basement high (Cullera positive anomaly) surrounded by a region with greater sedimentary cover (negative anomaly). This interpretation is further supported by the isopach maps derived from interpretation of the subsurface data (Fig. 5). The negative gravity anomaly correlates with an abrupt increase in the thickness of both the Pliocene and Quaternary sedimentary successions. Furthermore, the transitions in both the gravity anomaly and sedimentary thickness correspond to the positions of the main faults observed in the seismic dataset (see below). On the basis of this evidence, we propose that the southwestern Valencia Trough is structurally characterised by the presence of three major faults offsetting the basement and significantly influencing the stratigraphic evolution of the area. These three major faults are: the Cullera Fault, the Valencia Fault and the Albufera Fault (Fig. 5).

The structural configuration of the southwestern Valencia Trough is also influenced by the presence of Upper Triassic evaporites and shales at the base of the Mesozoic sedimentary cover. This mechanically weak layer induces tectonic decoupling within the seismogenic crust of the southwestern Valencia Trough. As a result, the deformation style of the suprasalt succession (cover) differs significantly from that of the subsalt succession (basement) (Etheve et al., 2018; Fang et al., 2021; Ramos et al., 2023, 2025; Roma et al., 2018).

The analysis of the seismic reflection profiles (Fig. 6) reveals three distinct fault types: i) faults restricted to the subsalt basement; ii) faults restricted to the

349 suprasalt cover; and iii) faults cutting through the sedimentary cover, basement and

350 salt layer.

351
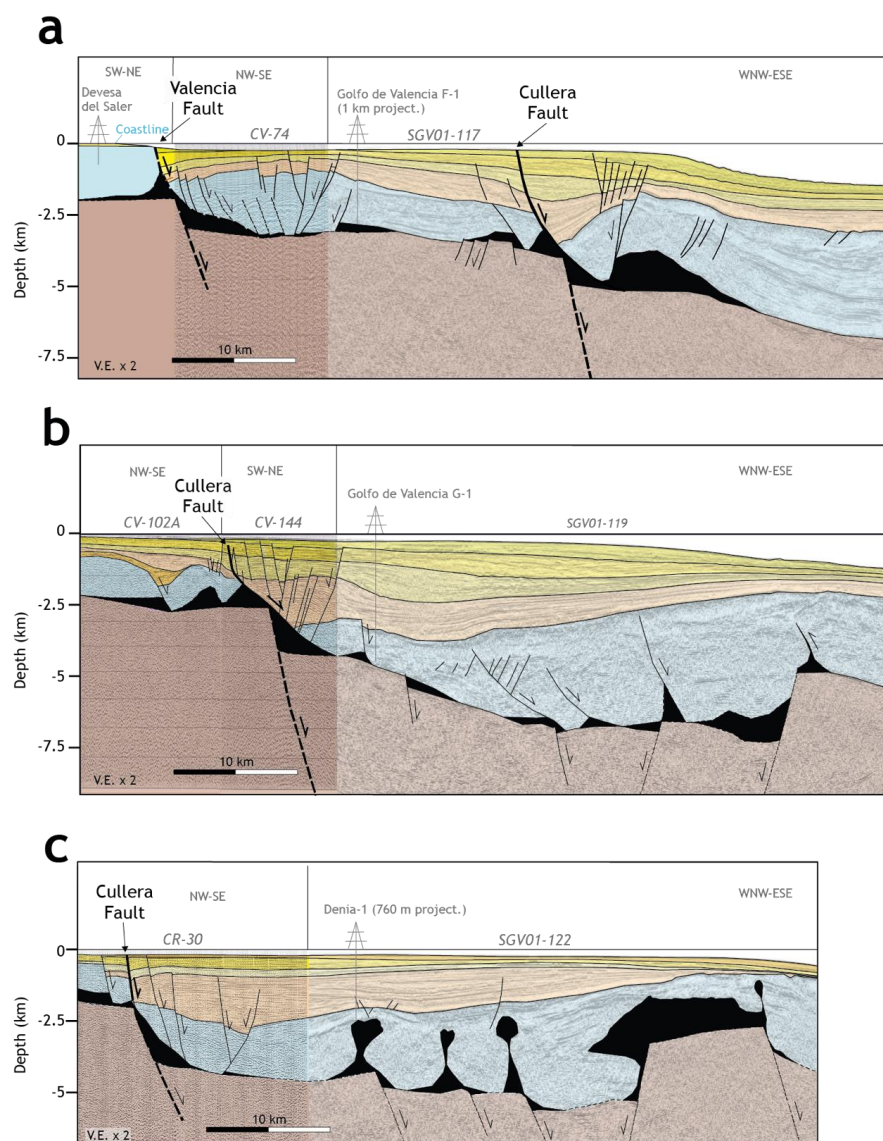
352
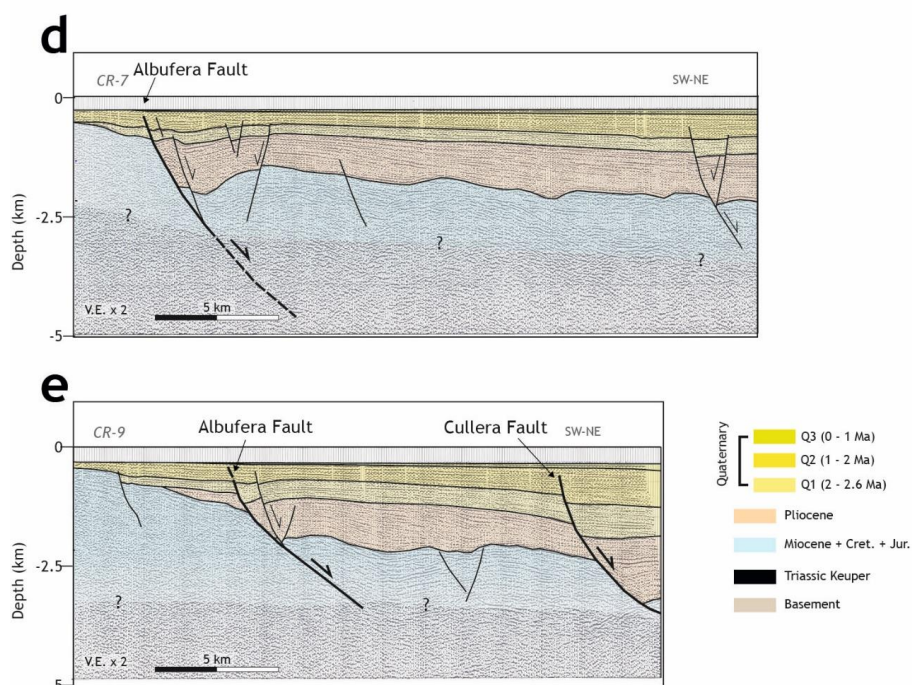
353

354   Fig. 6. Interpreted sections derived from onshore cross-sections (a) and the offshore

355   2D seismic profiles (a-e). See Fig. 3 for the location. a-c sections after Ramos et al.,

356   2025.

357

358   **5.1 Cullera Fault**

359   The Cullera Fault is the longest along-strike fault in the region, spans approximately

360   59 km, and has the highest cumulative offset, with more than 1800 m of vertical

361   displacement at the top of the Messinian horizon (Figs. 5 and 6).

362   The along-section geometry of the fault across the suprasalt succession is well

363   imaged in the seismic reflection dataset (Fig. 6). The Cullera Fault is a normal, NNE–

364   SSW-trending fault that dips highly towards the east. The fault offsets the entire

365   suprasalt cover, including the 1 Ma horizon. Owing to the low resolution of the

366   available bathymetric data, it is not possible to confirm whether the fault offsets the

367   seafloor. The Cullera Fault displaces the top of the basement horizon, indicating

368   that this fault involves both subsalt and suprasalt successions.

369 Within the basement, the Cullera Fault is poorly imaged in seismic profiles.

370 Nevertheless, the available data suggest that it is a planar fault (Fig. 6). This is also

371 supported by the absence of significant tilting of the basement-top horizon.

372 In contrast, the geometry of the Cullera Fault in the sedimentary cover is

373 heterogeneous. In the northern area (Fig. 6), the part of the Cullera Fault offsetting

374 the cover exhibits a listric geometry, which is responsible for the development of a

375 rollover structure in the hanging wall (Fig. 6). This listric geometry consists of a highly

376 dipping (50–60º) upper part offsetting the Plio-Quaternary succession and a gently

377 dipping (20–30º) lower part in the Mesozoic cover. Southwards, the listric geometry

378 and related rollover fold becomes less pronounced (Fig. 6).

379 To better constrain the geometry of the Cullera Fault, we constructed a structural

380 map of the fault by integrating fault traces identified in the seismic reflection dataset

381 with isopach maps (Fig. 7). Additionally, a 3D model of the Cullera Fault, along with

382 the two other major faults, was generated following a 2½D construction approach,

383 integrating interpreted seismic profiles via interpolation. We employed the ordinary

384 kriging algorithm implemented in MOVE software, a methodology consistent with

385 previous approaches applied to analogous structures (Ramos et al., 2020), ensuring

386 a geologically consistent representation of the fault geometry in the subsurface.

387 This approach allows for the reconstruction of complex fault surfaces by integrating

388 available geophysical data while minimising spatial uncertainties. Analysis of the

389 reconstructed 3D fault indicates that the surface area of the Cullera Fault offsetting

390 the sedimentary cover is approximately 360 km^2.

391
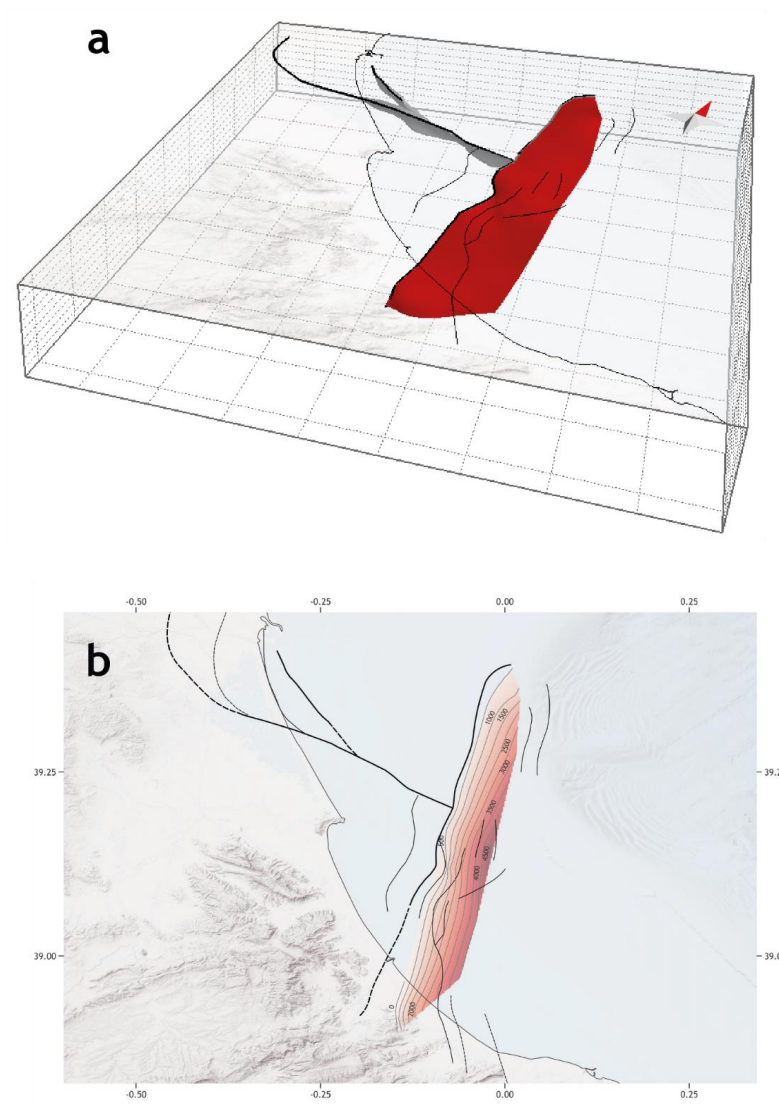
392

393 Figure 7. 3D model (a) and structural map (b) of the Cullera Fault (red surface).

394 Squares in figure a represent 10 km x 10 km. Note the red arrow pointing to the North

395 in figure a.

396

397 Several minor normal faults have developed in the hanging wall of the Cullera Fault

398 (Figs. 5). These faults displace only the suprasalt succession without affecting the

399   underlying subsalt units. In previous studies (e.g., Perea 2006; Roca 1992) distinct

400   names were assigned to these faults, such as the Western Cabo Cullera Fault,

401   Central Cabo Cullera Fault, and Eastern Cabo Cullera Fault. However, the improved

402   resolution and quality of the new seismic dataset enable a more detailed

403   characterisation of these tectonic structures, allowing for a reassessment of their

404   nomenclature and role. On the basis of our analysis, we interpret these minor faults

405   to be part of the damage zone associated with the main Cullera Fault. Fault damage

406   zones typically consist of subsidiary structures that develop in response to the

407   distribution of strain surrounding a major fault. In this context, these minor faults

408   represent secondary features that contribute to the overall deformation but are

409   structurally subordinate to the Cullera Fault. Consequently, we propose

410   consolidating the nomenclature to avoid potential confusion. Instead of assigning

411   separate names to these subsidiary faults, we retain the term Cullera Fault

412   exclusively for the main structure.

413   The quality of the seismic dataset in profiles GV-102A and SGV-117 (Fig. 3) allows for

414   an analysis of the slip rate of the Cullera Fault. This analysis is approximate,

415   because of the resolution of the seismic profiles, the uncertainties in the recognition

416   of the markers in the hanging wall and footwall, and the age of these markers. Net

417   slip rates were obtained for the Top-Messinian, Top Pliocene, Top-Q1, and Top-Q2

418   horizons, with assigned ages of 5.3 Ma, 2.6 Ma, 2 Ma, and 1 Ma, respectively.

419   Analogous values of the slip rate for each of these markers were obtained from the

420   two analysed seismic profiles (Fig. 8). The slip rates for the Cullera Fault seem to

421   have decreased over time, as the calculation yielded mean slip rates of 0.40 ± 0.1

422   mm/y for the Pliocene and 0.15± 0.1 mm/y for the Quaternary. However, we cannot

423   dismiss that this apparent in-time evolution could be an artefact related to the

424   epistemic uncertainties mentioned above.
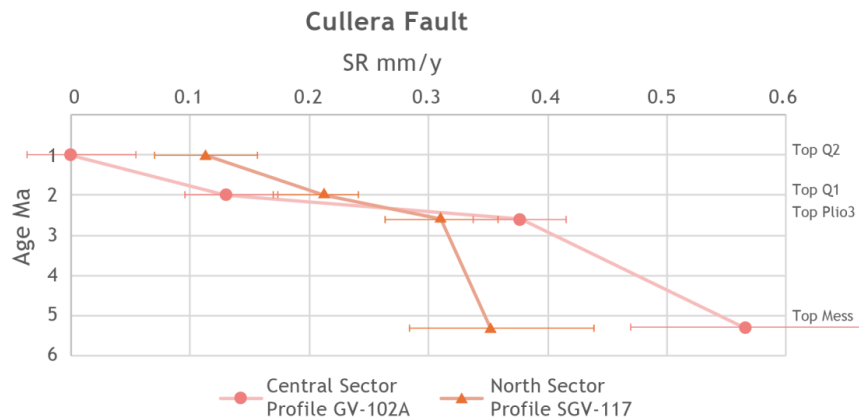
Figure 8. Long term slip rates (SR) for the Cullera Fault derived from the seismic profiles for the Top Messinian, Top Plio3, Top Q1, and Top Q2 horizons. Pink line and dots represent SR for the central sector of the fault. Orange line and triangles indicate SR for the north sector of the fault. Slip rates seem to decrease in time, from 0.40 ± 0.1 mm/y for the Pliocene to 0.15± 0.1 mm/y for the Quaternary. Error bars are estimated on the basis of uncertainties in the recognition of the markers and their ages.

5.2. Albufera Fault

The Albufera Fault (F3) (Figs. 5 and 6) is a newly defined active structure in the southwestern Valencia Trough. This NW–SE striking fault extends approximately 55 km and exhibits a maximum normal offset of 1000 m for the Top-Messinian horizon. This would imply a long-term slip rate of 0.2 ± 0.1 mm/y. The fault offsets both the supra- and subsalt successions (Figs. 5 and 6). The Albufera Fault is visible only in the vintage seismic reflection dataset, where it presents a low dip and a listric geometry.

The Albufera Fault appears to offset the entire suprasalt cover, including the 1 Ma horizon. As with other faults in the region, the low resolution of the available bathymetric data prevents us from determining whether this fault offsets the seabed. Nevertheless, high-resolution seismic profiles from the offshore shelf analysed by previous authors indicate seabed offsets caused by secondary normal

447   faults likely associated with the Albufera Fault (Díaz de Río et al., 1986; Albarracín

448   et al., 2013).

449   The available seismic dataset reveals a normal kinematic component for the

450   Albufera Fault. However, mapping of small-scale fault traces in upper Pleistocene–

451   recent sediments (interval between the seabed and the 1.8 Ma horizon) reveals that

452   these faults are oblique to the main trend of the Albufera Fault, forming an en

453   echelon pattern in map view, which suggests that the Plio-Quaternary reactivation

454   of the main fault has a significant right-lateral strike-slip component. This dextral

455   component along the NW–SE trending fault is consistent with the regional ENE–

456   WSW direction of Plio-Quaternary extension in the southwestern Valencia Trough

457   and kinematically consistent with NNW–SSE trending normal faults. The fault

458   influences the Plio-Quaternary sedimentary infill of the southwestern Valencia

459   Trough (Fig. 5). The computed isopach maps reveal that the Pliocene succession

460   significantly increased in the hanging wall relative to the footwall. Similarly, the

461   Quaternary succession is thicker in the hanging wall than in the footwall. The listric

462   geometry of the Albufera Fault is responsible for the development of a rollover

463   anticline in the hanging wall (Fig. 6). This anticline is likely accentuated by the

464   palaeoshelf edge of the late Tortonian–early Messinian shelf, which is located in the

465   central part of the rollover structure.

466   To further constrain the geometry of the Albufera Fault, a structural map of the

467   fault was constructed (Fig. 9). Analysis of the reconstructed 3D fault surface

468   indicates that the fault encompasses an area of approximately 560 km^2.
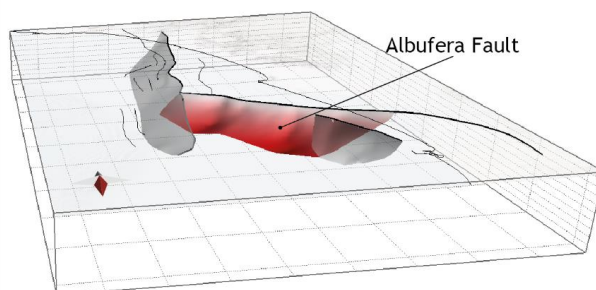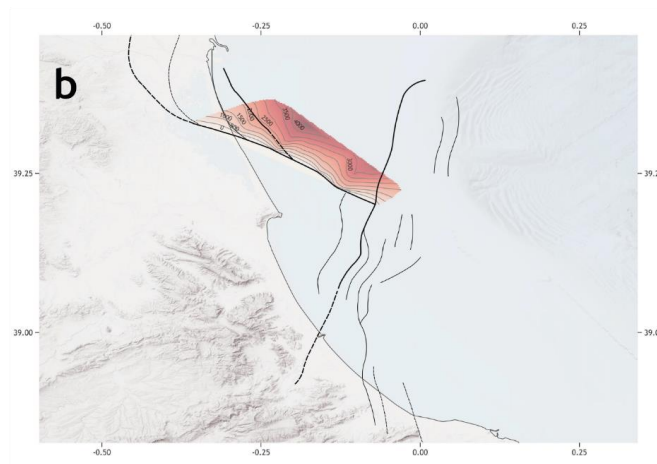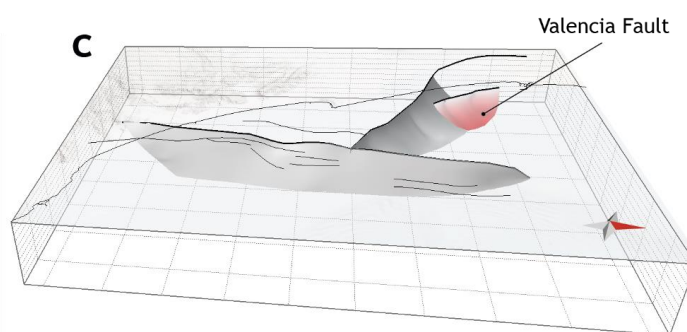
469

470

471

472

473

474

475

476

477
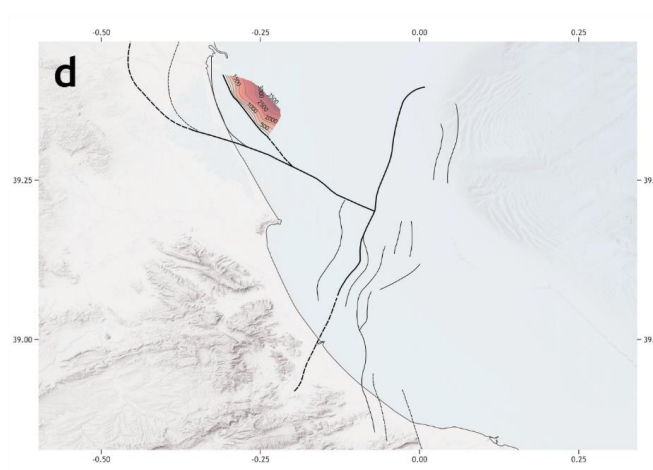
Figure 9. 3D model and structural map of the Albufera Fault (a and b) and the Valencia Fault (c and d). Squares in 3D models represent 10 km x 10 km. Note the red arrow pointing to the North in figures a and c.

5.3 Valencia Fault

In this section, we define for the first time the Valencia Fault (Figs. 5 and 6). This structure is considered one of the main active faults in the southwestern Valencia Trough because of its length of approximately 20 km and its significant impact on the distribution of Quaternary depocentres. The Valencia Fault displaces both the supra- and subsalt successions (see below) (Figs. 5 and 6).

This NNW–SSE trending, steeply dipping fault is imaged primarily in the vintage seismic reflection dataset, where it exhibits a listric geometry, at least in the portion offsetting the suprasalt succession (Fig. 6). The Valencia Fault offsets the entire suprasalt cover, including the 1 Ma horizon. However, owing to the low resolution of the available bathymetric data, it is not possible to determine whether this fault offsets the seabed. The Valencia Fault also displaces the top of the basement horizon, indicating that this structure involves both subsalt and suprasalt successions. Within the basement, the Valencia Fault is not well-imaged in the

498   seismic profiles, but the absence of tilting in the basement-top horizon suggests

499   that it is a planar fault (Fig. 6). The Valencia Fault and its secondary strands very

500   likely continue onshore below the City of Valencia. The lack of onshore seismic data

501   hampers the mapping of these fault strands, but their presence can be inferred from

502   the abrupt Plio-Quaternary thickness changes observed in water wells and Vertical

503   Electric Sounding profiles.

504   To further constrain the geometry of the Valencia Fault, a structural map of the fault

505   was constructed (Fig. 9). Analysis of the reconstructed 3D fault surface indicates

506   that the fault encompasses an area of approximately 208 km^2.

507

6. Evolutionary growth of the Cullera Fault: interplay between tectonics and salt withdrawal.

This section aims to provide further insights into the evolution of the active faults in the southwestern Valencia Trough. The low resolution of the vintage seismic dataset limits the ability to perform a detailed analysis only for the Cullera Fault. To analyse recent along-dip variations in throw, we constructed throw-depth plots (T-z plots) for the post-Messinian markers (Fig. 10). These plots provide insights into the evolutionary growth of the fault (Mansfield and Cartwright, 1996; Hongxing and Anderson, 2007). The quality of the available seismic reflection dataset allows this analysis to be performed on two seismic profiles located in the northern part of the fault, where the listric geometry is well-developed (LINES SGV01-115 and SGV01-117; Fig. 6).

We computed T-z plots for six suprasalt horizons: Top-Messinian, Top Plio1, Top Plio2, Top Plio3, Top Q1, and Top Q2 (Fig. 10). The T-z plots for the Cullera Fault reveal a general increase in the throw and throw gradient with depth. However, the data indicate two distinct portions with differing throw gradients: (i) the lower portion, with higher throw gradients, includes horizons from the Top Messinian to the Top Pliocene; (ii) the upper portion, with lower throw gradients, comprises the Quaternary horizons. This distinction between these two portions is particularly pronounced in the southern seismic line (line SGV01-117, Fig. 6). Here, the throw gradient decreases, from 2.38-2.98 in the lower portion to 0.22-0.10 in the upper portion.
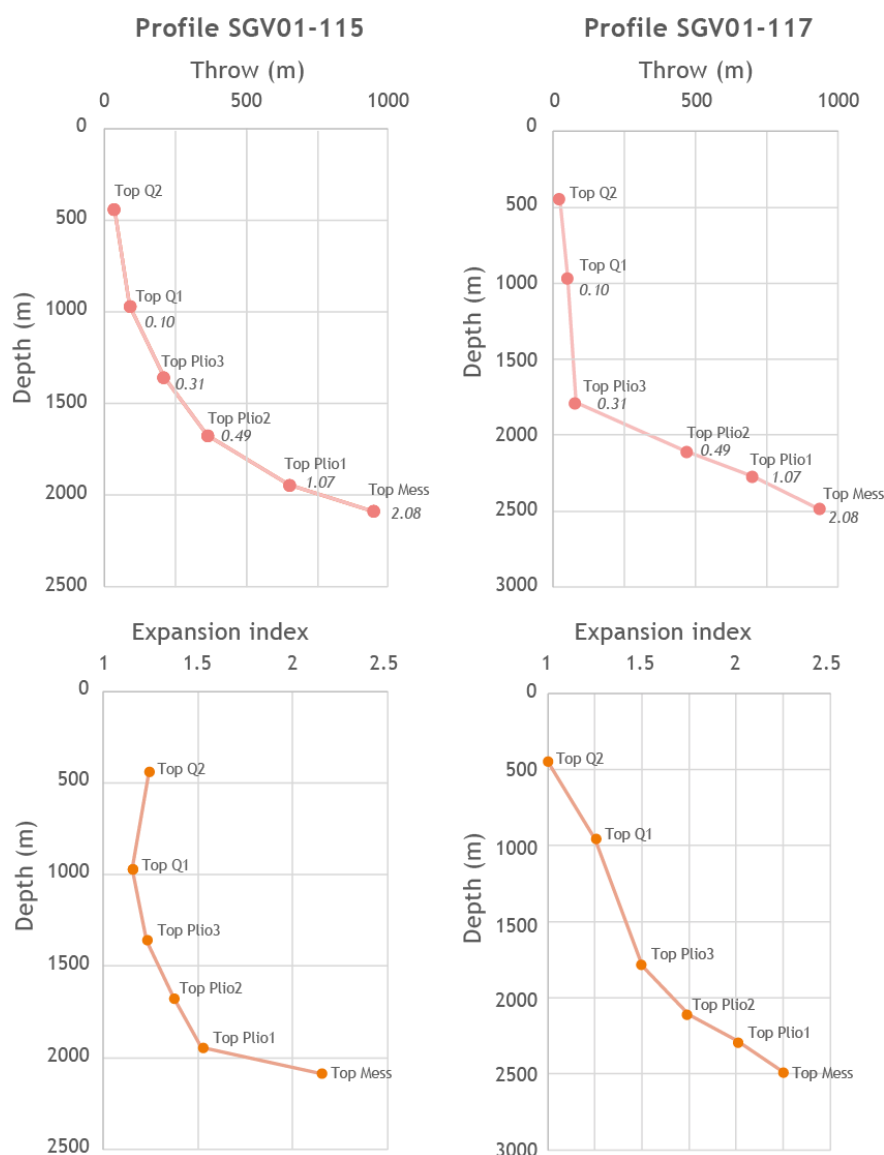
Figure 10. Throw depth (T-z) and expansion index plots for the Cullera Fault computed from profiles SGV01-115 and SGV01-117. The numbers within the T-z plots indicate the throw gradient for the corresponding interval. The T-z plots reveal an increase in the throw and throw gradient, with a higher throw gradient for the Top Messinian–Top Pliocene interval and a lower throw gradient for the Quaternary interval.

The Cullera Fault significantly influences the Plio-Quaternary sedimentary infill of the southwestern Valencia Trough. Isopach maps indicate a marked increase in the thickness of both Pliocene and Quaternary successions in the hanging wall with respect to the footwall (Fig. 5). This thickness variation offers critical insights into the history of fault growth. To quantify this relationship, we computed the expansion index (Thorsen, 1963; Rouby et al., 2003; Jackson and Rotevatn, 2013) for the post-Messinian stratigraphic units (Fig. 10). The expansion index consistently exceeds 1 across all the analysed intervals, indicating a synkinematic deposition in these units. Notably, the Pliocene units exhibit a greater expansion index than the Quaternary units do, with the difference being particularly pronounced in the southern seismic line (Fig. 6 LINE SGV01-117).

Finally, to shed light on the mechanisms controlling the creation of accommodation space related to the Cullera Fault, we analyse the tectonic–stratigraphic arrangement of the hanging wall units. In the northern part of the Cullera Fault, where the rollover structure is well developed (Fig. 6), the position of the Plio-Quaternary depocenter in the hanging-wall varies along the dipdirection. The Pliocene depocentre remains in the immediate hanging wall of the fault. However, during the deposition of unit Q1, the depocentre migrated basinwards. The depocentre of unit Q2 is located adjacent to the fault, whereas the depocentre of unit Q3 is located further east, related to the progradational geometry of the sedimentary bodies. Nevertheless, when focusing strictly on the area affected by the fault, the local Q3 depocentre also remains adjacent to the fault.

Analogous stratigraphic geometries have been observed in the Danish North Sea, where they have been interpreted in terms of the evolution of a salt-influenced fault (Duffy et al., 2023 and references therein). In such a setting, two mechanisms create accommodation space: fault displacement and load-driven salt withdrawal in the hanging-wall. These two mechanisms can act separately or contemporaneously in time. When the accommodation space generated by the fault offset exceeds that created by salt withdrawal, the depocentre axis remains adjacent to the fault. In contrast, when salt-related accommodation space is dominant, the depocentre migrates away from the fault (Duffy et al., 2023).

568   Accordingly, we interpret that, during the Pliocene, the accommodation space

569   generated by the displacement of the Cullera Fault exceeded that produced by the

570   accommodation space related to salt withdrawal, as evidenced by the depocentre's

571   axis being located adjacent to the fault (Fig. 6). During the deposition of unit Q1, the

572   depocentre migrated basinwards, suggesting that salt withdrawal-related

573   accommodation space outpaced that related to fault displacement. Finally, during

574   Q2 and Q3, the depocentre axis shifted towards the fault, indicating that fault

575   displacement-related accommodation space regained dominance over salt

576   mobility.

577   All the above-described features shed light on the evolution of the salt-influenced

578   Cullera Fault. As previously discussed, the creation of accommodation space

579   results from two mechanisms: tectonic offset along the fault and displacement

580   related to salt withdrawal. Both mechanisms act cumulatively; that is, both

581   mechanisms produce slip along the Cullera Fault and create accommodation

582   space. The migration of successive depocentres suggests that, during the Pliocene,

583   accommodation space related to tectonic offset was greater than that created by

584   salt withdrawal. As, the throw gradient is high (≈ 2.4) during this period, we postulate

585   that both mechanisms were active. During the deposition of Q1 (2.6–2 Ma), the

586   position of the depocentre suggests that salt mobility became the dominant

587   mechanism, likely due to a decrease in fault activity, an increase in salt withdrawal,

588   or both. As the throw gradient decreases during this period, we postulate that a

589   decrease in the fault displacement rate could be the reason for the change in the

590   main mechanism. Finally, during the rest of the Quaternary (2 Ma to present), fault

591   displacement-related accommodation space once again exceeded that created by

592   salt withdrawal. The constant throw gradient observed during this period with

593   respect to the previous time interval (2.6–2 Ma) suggests that the change in the main

594   mechanism was due to a reduction in or cessation of salt withdrawal. This

595   interpretation is further supported by the off-fault geometry of the Q2–Q3

596   sedimentary bodies, as no significant change in thickness is observed above the salt

597   withdrawal-related anticlinal crest located east of the Cullera Fault (Fig. 6).

598   Therefore, the evolution of the Cullera Fault during the Pliocene–Quaternary time

599   span was controlled mainly by the tectonic offset, except for the time interval

600   between 2.6 and 2 Ma, when offset was related mainly to salt withdrawal.

601

7. Influence of mechanical layering on the seismic potential: the case of the southwestern Valencia Trough

The southwestern Valencia Trough has a distinct mechanical stratigraphy characterised by a subsalt basement and a suprasalt Mesozoic–Quaternary sedimentary succession. These two units are separated by a weak mechanical layer composed of Triassic evaporites. These lithologies are well documented for their ductile behaviour, which enables them to act as regional detachment layers (e.g., Morley et al., 2003; Jackson and Hudec, 2005) and inhibits the propagation of faults (e.g., Withjack et al., 1990; Pascoe et al., 1999; Maurin and Niviere, 2000; Withjack and Callaway, 2000; Richardson et al., 2005; Ford et al., 2007; Kane et al., 2010; Marsh et al., 2010). Moreover, mechanically weak layers have been shown to induce full or partial geometric and kinematic decoupling between sub- and supradetachment successions (e.g., Stewart et al., 1997; Withjack and Callaway, 2000; Ford et al., 2007; Tvedt et al. 2013). In this section, we focus on the implications of this mechanical arrangement in terms of the seismic potential of salt-influenced active faults.

In an active region, tectonics are generally the main driving mechanism of fault displacement. However, in the case of salt-influenced faults, displacement can also result from salt withdrawal. Our analysis of the evolution of the Cullera Fault presented in the previous section indicates that the fault offset is related to the interplay between two mechanisms: tectonic offset along the fault and displacement related to salt withdrawal. Our analysis also reveals how these two processes interact with each other. Consequently, in areas with salt-influenced faults, seismicity can potentially be produced from either mechanism or a combination of both.

In terms of seismic potential, there is a significant difference between a tectonic earthquake and a salt-withdrawal earthquake. This difference lies in the maximum potential thickness of the seismogenic layer involved in the rupture. A tectonically driven earthquake could theoretically rupture the entire seismogenic crust. In contrast, a salt withdrawal-related earthquake would imply offset restricted to the suprasalt succession. Therefore, in an earthquake restricted to the suprasalt

633   succession, the thickness of the seismogenic layer is limited by the depth of the

634   mechanically weak layer, reducing the maximum potential rupture area and,

635   consequently, the seismic potential. A salt-withdrawal-related earthquake could

636   induce a vertical stress drop related to salt displacement, potentially triggering

637   displacement in the subsalt succession and leading to a complex rupture. However,

638   in terms of seismic potential, such a hypothetical earthquake would not differ from

639   a tectonically-driven event. Similarly, a tectonically driven earthquake may rupture

640   only the suprasalt succession.

641   Despite the mechanism driving seismicity, the presence of a weak mechanical layer

642   within the seismogenic crust significantly influences the seismogenic potential of

643   active faults. We hypothesise that this weak layer could locally hinder the effective

644   vertical propagation of a rupture, thereby resulting in faults being seismogenically

645   bonded. Specifically, the total or partial decoupling induced by the weak evaporitic

646   layer may limit the effective width of the seismogenic layer. This hypothesis is

647   independent of the weak layer composition; therefore, our hypothesis can be

648   extended to any region with a similar structural configuration.

649   A widely used approach to characterise the seismic potential of an active fault

650   involves earthquake fault scaling relationships. These relationships estimate the

651   seismic parameters of an active fault on the basis of its geometric and/or kinematic

652   features (Kanamori and Anderson, 1975; Geller, 1976; Wells and Coppersmith;

653   1994; Stirling et al., 2002 and 2013; Leonard, 2010 and 2014; among many others).

654   In the case of the southwestern Valencia Trough faults, the available data support

655   characterisation on the basis of geometric features, such as fault area, length, or

656   width. However, the mechanical layering observed in the southwestern Valencia

657   Trough necessitates the cautious application of these scaling relationships. The

658   influence of the weak mechanical layer introduces complexities that may not be

659   fully accounted for by traditional scaling methods.

660   Therefore, we begin our analysis by comparing the southwestern Valencia Trough

661   with the Zagros fold-and-thrust belt. While Zagros fold-and-thrust belt differs

662   tectonically from the southwestern Valencia Trough, as it is dominated by

663   shortening rather than extension, it structurally resembles the southwestern

664   Valencia Trough because of its pronounced mechanical layering in the upper crust.

665   The Zagros fold-and-thrust belt features a crystalline basement overlain by a 10-km-

666   thick Precambrian–Quaternary sedimentary cover. These two successions are

667   separated by the Hormuz salt layer (Casciello *et al.* ,2009; Sherkati *et al.;* 2005;

668   Molinaro *et al.,* 2005). That is, similar to the southwestern Valencia Trough, the

669   seismogenic crust is characterised by the presence of an intermediate

670   mechanically weak layer. Seismicity in the Zagros fold-and-thrust belt is

671   characterised by a general absence of coseismic surface ruptures. This seismicity

672   nucleates both in the basement and in the cover (Nissen et al., 2011). Notably, the

673   centroids of most of the larger events (magnitudes exceeding Mw 5), are located at

674   depths between 4 and 14 km, indicating that seismic activity nucleates both within

675   the suprasalt succession and in the basement (Nissen et al. 2007, 2010; Roustaei

676   et al. 2010). Additionally, very large earthquakes have occurred in the Zagros fold-

677   and-thrust belt; these earthquakes include the Ghir and Khurgu events (M_w=6.7),

678   which are interpreted as ruptures involving both the basement and the cover,

679   rupturing through the basement–cover interface (Nissen et al., 2011).

680   We propose that the southwestern Valencia Trough may exhibit a comparable

681   pattern of seismicity to that of the Zagros fold-and-thrust belt. Specifically, we

682   hypothesise that seismic events in the southwestern Valencia Trough could have

683   nucleated within both the basement and the suprasalt succession. Furthermore, we

684   postulate that larger earthquakes in the southwestern Valencia Trough could also

685   rupture both mechanical layers. Available centroid data for the southwestern

686   Valencia Trough suggest that most earthquakes nucleate at depths between 1 and

687   13 km (Fig. 2). Although these depth estimates carry significant uncertainties, we

688   interpret this dataset as supporting evidence for our hypothesis that seismicity in

689   the southwestern Valencia Trough nucleates both in the basement and in the cover.

690   As we mentioned previously, most empirical source-scaling relationships for crustal

691   earthquakes correlate the moment magnitude (Mw) with the fault dimensions

692   (length, width, and/or area; (Kanamori and Anderson, 1975; Geller, 1976; Wells and

693   Coppersmith; 1994; Stirling et al., 2022; Leonard, 2010; among many others). We

694   propose that when these scaling relationships are applied to regions with a weak

695   mechanical layer, the role of this layer should be explicitly considered in the
696   analysis. This is because the presence of a weak layer can potentially hinder the
697   effective vertical propagation of a rupture, thereby limiting the effective width of the
698   seismogenic layer. This consideration is particularly relevant for earthquakes that
699   nucleate above the weak layer.

700   Several studies suggest that the downdip width of the seismogenic crust (the
701   thickness of seismogenic crust measured along the fault plane) can constrain the
702   maximum magnitudes of earthquakes (Hyndman, 2007; Ruff and Kanamori, 1983;
703   Weng & Yang, 2017). For large-magnitude events involving the entire seismogenic
704   crust, some scaling relationships account for the constraint on fault-width rupture
705   growth relative to fault-length rupture growth by incorporating a change in slope in
706   width-to-length scaling (Leonard, 2010; Yen and Ma, 2011; Leonard, 2014; Cheng et
707   al., 2019; Huang et al., 2024). This change in slope reflects the width of the
708   seismogenic crust, which imposes a limit on rupture propagation owing to
709   variations in the mechanical behaviour of the crust. We propose a similar approach
710   to evaluate the seismic potential of regions characterised by a weak mechanical
711   layer within the upper crust, such as the southwestern Valencia Trough.

712   Our approach involves including the rupture aspect ratio when calculating the
713   geometric parameters of an active fault. Specifically, we propose that, instead of
714   using the total area or length of the fault as direct inputs to scaling relationships, a
715   correction factor should be applied to these geometric parameters. This correction
716   factor is based on the empirical aspect ratio of faults. For example, consider an
717   earthquake nucleating above a weak mechanical layer. Two potential scenarios for
718   the propagation of such an earthquake can be envisioned: i) that it propagates
719   through the basement–cover interface or ii) that it remains restricted to the
720   succession above the weak layer. In the first scenario, the potential maximum
721   rupture area can be calculated by multiplying the fault length by the fault width. Any
722   area-based or length-based scaling relationship can then be applied. This scenario
723   represents the maximum seismic potential of the fault.

724   In the second scenario, where rupture propagation is restricted to succession above
725   the weak layer, a simplistic calculation of the fault area would multiply the total fault

726   length by the thickness of the ruptured succession (Fig 11). However, since the

727   hypothesised rupture offsets only the succession above the mechanically weak

728   layer, the width of the rupture is significantly limited. This would result in a highly

729   elongated rupture with an unusually high aspect ratio, deviating from commonly

730   observed values (Nicol et al., 1996; Stock & Smith, 2000). For this second scenario,

731   we propose using the thickness of the ruptured succession as a limiting factor.

732   Specifically, the rupture area should be calculated by multiplying the width of the

733   fault offset (based on the thickness of the succession above the weak layer and

734   corrected by the fault dip) by the total fault length weighted by the aspect ratio (Fig

735   11). This weighted area can then be used as input in any area-based scaling

736   relationship. We consider that this calculation offers a more realistic estimation of

737   the maximum seismogenic potential for events rupturing only the succession above

738   the weak layer. Finally, we recommend avoiding length-based scaling relations for

739   this second scenario, as such relations implicitly assume a rupture of the entire

740   seismogenic crust.

741
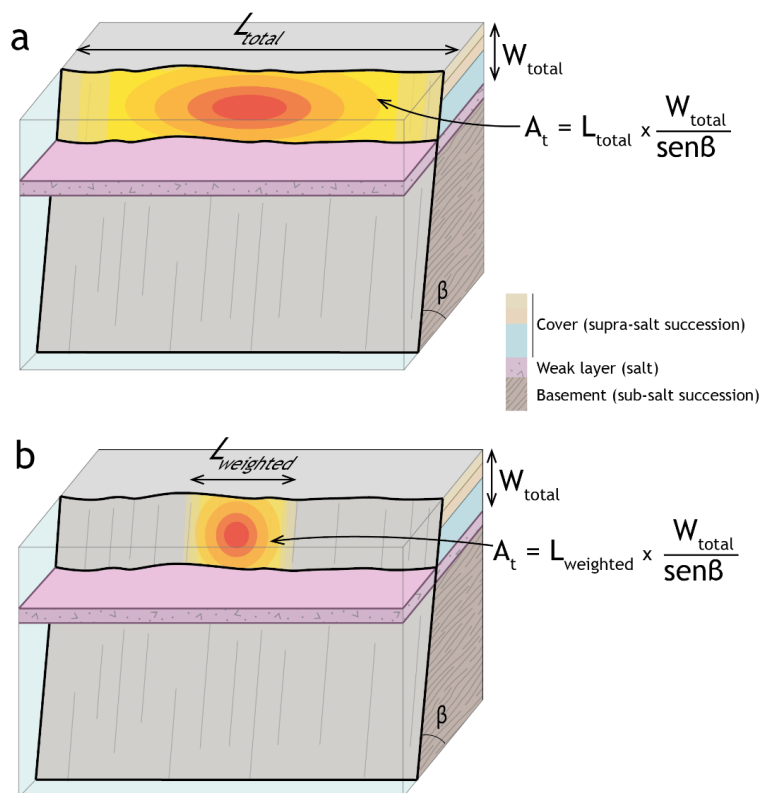
Figure 11. Conceptual model of the weighted rupture area of an earthquake nucleating above the weak mechanical layer. The area of the rupture is shown using a red–yellow gradient. An earthquake rupturing the total fault length (L) and the total thickness (W_{total}) above the weak layer would result in nonrealistic, highly elongated ruptures. In figure panel b, we propose a more realistic case: an earthquake offsetting the total thickness above the weak layer (W_{total}) and a rupture length weighted by the aspect ratio (L_w).

749

750

8. Seismic characterisation of active faults in the southwestern Valencia Trough.

In this section, we compute the seismic potential of the active faults in the southwestern Valencia Trough by applying several scaling relationships. We perform two distinct calculations corresponding to the two scenarios described earlier. i) In the first scenario, we assume a rupture involving both the supra- and subsalt successions. That is, this first scenario accounts for an earthquake rupturing the entire seismogenic crust. This scenario provides the maximum seismic potential of the faults. ii) In the second scenario, we assume that a rupture is restricted to the suprasalt succession. For this calculation, we apply several area-based scaling relationships, and we use the area weighted by the aspect ratio as the input parameter. Since the rupture area involved in this second scenario is relatively small, a relatively low seismogenic potential is expected.

8.1. First scenario: Ruptures involving the entire seismogenic crust.

For both scenarios, we apply the scaling relationships of Wells & Coppersmith (1994) (values corresponding to normal faults) and Stirling et al. (2002). In the first scenario, i.e., ruptures involving the entire seismogenic crust, we assume that a complete fault ruptured from the subsalt basement through the suprasalt succession. Since the total thickness of the seismogenic crust is not precisely known, we used the fault length as the primary input parameter for these calculations (Table 1).

Table 1 Source parameters obtained from scaling relationships (Wells & Coppersmith, 1994 -WC94- and Stirling et al., 2002 -Stirling02-) assuming ruptures involving the entire seismogenic crust.

	Input parameters	WC94			Stirling02	
	L km	M_W	AD m	MD m	M_W	AD m
Cullera Fault	59	7.2 ±0.34	1.61 ±0.37	4.94 ±0.41	7.3 ±0.30	2.39 ±0.24
Albufera Fault	20	6.58 ±0.34	0.42 ±0.37	0.97 ±0.41	6.92 ±0.30	1.97 ±0.24
Valencia Fault	40	6.97 ±0.34	0.99 ±0.37	2.75 ±0.41	7.16 ±0.30	2.23 ±0.24

778

779 *8.2. Second scenario: Ruptures involving only the suprasalt succession*

780 In this scenario, the presence of a mechanically weak layer within the seismogenic

781 crust is considered to control the seismic potential of active faults. As discussed

782 previously, we use the weighted rupture area as the input parameter for the scaling

783 relationships. The weighting factor is based on the aspect ratio of normal faults. To

784 provide context for this approach, we also present seismic parameters calculated

785 from the total fault area offsetting the entire suprasalt succession. The aspect ratios

786 of normal fault ruptures vary widely (0.4–18); however, most of the observed

787 ruptures are within the range of 0.5 to 3.5 (Nicol et al., 1996; Stock & Smith, 2000),

788 with a mode value of 1.8 (30%, Stock & Smith, 2000). Numerical simulations of

789 strike-slip faults by Weng & Yang (2016) demonstrated that the width of the

790 seismogenic layer significantly influences the rupture aspect ratios. According to

791 their findings, a seismogenic layer thickness of approximately 10 km marks a critical

792 boundary: for thicknesses less than this value, rupture aspect ratios remain low (ca.

793 2), whereas thicknesses greater than 10 km result in significantly higher aspect

794 ratios (<8). Considering these findings and given that the suprasalt succession in the

795 southwestern Valencia Trough has an average thickness of approximately 5 km, we

796 adopt an aspect ratio of 1.8 for our calculations.

797   In the southwestern Valencia Trough, the suprasalt succession thickness (~5 km)

798   and an average fault dip of ~45° yield a maximum rupture width of approximately 7.1

799   km for events confined to the suprasalt succession. For events unrestricted by the

800   aspect ratio (i.e., earthquakes rupturing the entire fault length and width of the

801   suprasalt succession), we compute the rupture area as the product of length and

802   width (L*W). However, when the seismic potential for ruptures weighted by the

803   aspect ratio is calculated, the controlling factor is the fault width. As we assume a

804   constant thickness for the suprasalt succession across southwestern Valencia

805   Trough, the rupture area and corresponding seismic potential are consistent for all

806   the faults in this study (Table 2).

807

808   Table 2 Moment magnitude obtained from scaling relationships (Wells &

809   Coppersmith, 1994 -WC94- and Stirling et al., 2002 -Stirling02-). The first column

810   (not weighted area) corresponds to the values obtained assuming ruptures involving

811   the total suprasalt succession. The second column (weighted area) shows the

812   values obtained using the area weighted by the aspect ratio as input parameter.

	Not weighted area			Weighted area		
	Input parameters A km^2	M_W WC94	M_W Stirling02	Input parameters A km^2	M_W WC94	M_W Stirling02
Cullera Fault	511.4	6.69 ±0.34	7.07 ±0.26	135.2	6.10 ±0.34	6.65 ±0.26
Albufera Fault	346.7	6.21 ±0.34	6.72 ±0.26	135.2	6.10 ±0.34	6.65 ±0.26
Valencia Fault	173.4	6.52 ±0.34	6.94 ±0.26	135.2	6.10 ±0.34	6.65 ±0.26

813

814   The comparison between the standard application of earthquake source scaling
815   relations and the approach presented here for regions characterised by the
816   presence of a weak mechanical layer within the seismogenic crust reveals
817   significant differences (Fig. 12). The maximum expected magnitudes for
818   characteristic events rupturing the entire seismogenic crust (i.e., propagating
819   across the basement–cover interface) are estimated to be 7.2–7.3, 6.58–6.92, and
820   6.97–7.16 for the Cullera, Valencia, and Albufera Faults, respectively. In contrast, for
821   hypothetical earthquakes restricted to the suprasalt succession and rupturing of
822   the total length of the faults, the expected magnitudes are lower, ranging from 6.7–
823   7.1, 6.2–6.7, and 6.5–6.9 for the Cullera, Valencia, and Albufera faults, respectively.
824   However, in such cases, we argue that the seismic potential derived using area-
825   weighted relations provides a more realistic estimate. Using this approach, our
826   calculations yield maximum magnitudes of 6.1–6.7 for all faults. These values are
827   2–9 % lower than those obtained when accounting for the total suprasalt
828   succession thickness.

829   When the area-weighted values are compared with the maximum expected
830   magnitudes for ruptures involving the entire seismogenic crust, the results reveal a
831   4–15% reduction. This discrepancy highlights the importance of incorporating
832   mechanical layering into seismic potential assessments in regions where weak
833   layers influence fault dynamics and rupture propagation. Furthermore, these
834   differences in seismic potential should be addressed in probabilistic seismic hazard
835   assessments.

836
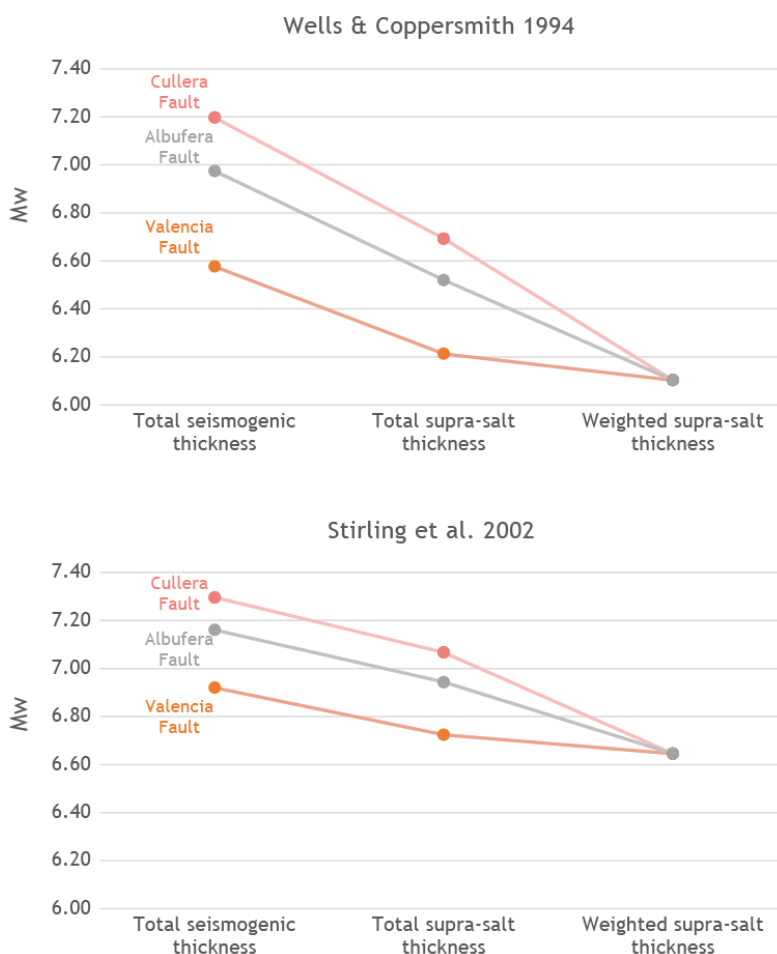
Figure 12. Plots of M_w values for the Cullera, Albufera and Valencia Faults obtained using the scaling relationships of Wells & Coppersmith (1994) and Stirling et al. (2002). The plots show the values computed assuming a rupture of the total seismogenic thickness, a rupture of the total suprasalt succession, and the values assuming a rupture of an area calculated using a suprasalt thickness weighted with the aspect ratio.

843

9. Conclusions.

Analysis of a comprehensive subsurface dataset from the southwestern Valencia Trough enables the identification of three major active normal faults: the Cullera, Albufera and Valencia faults. Among these faults, the Cullera Fault is the main active structure in this region, with a cumulative offset of 1800 m at the top of the Messinian marker. The long-term slip rate varies over time between 0.15 ±0.1 mm/y and 0.4 ±0.1 mm/y. The Albufera Fault, which is 55 km in length, has a long-term slip rate of 0.2 ±0.1 mm/y, whereas the 20-km-long Valencia Fault significantly influences the spatial distribution of Quaternary depocentres.

Our results also reveal heterogeneous seismogenic crust in the study area, largely because of a mechanically weak layer, which is composed mainly of Triassic evaporites. Consequently, two competing mechanisms are responsible for the offset along the active faults: tectonics and salt withdrawal. A quantitative evolutionary analysis of the Cullera Fault indicates that tectonics was the dominant mechanism during the Pliocene, whereas salt withdrawal took precedence in the early Quaternary (2.6–2 Ma). After 2 Ma, tectonic activity once again became the primary driver of fault displacement.

The mechanically layered crust of the southwestern Valencia Trough influences seismicity: events may nucleate in either the basement or the suprasalt succession. Total or partial decoupling related to the mechanically weak layer implies that an earthquake that nucleated in the suprasalt succession would likely be restricted to this upper part of the seismogenic crust, yet larger events involving basement and cover units are also plausible. For reliable seismic hazard assessments, both scenarios must be accounted for. To compute the seismogenic potential of active faults under the assumption of rupture within the suprasalt succession, we propose the use of the rupture aspect ratio as a correction factor for the maximum rupture area. Specifically, the product of the suprasalt thickness (corrected by the fault dip) and the fault length—weighted by the aspect ratio—provides a more realistic approximation of the maximum rupture area. Using this method, the maximum magnitudes for suprasalt ruptures are 2–9% lower than those obtained by

874   considering the full suprasalt thickness alone, and 4–15% lower than estimates

875   involving the entire seismogenic crust.

876   Overall, these findings greatly enhance our understanding of the seismogenic

877   potential of the southwestern Valencia Trough, an offshore area near densely

878   populated areas. These findings provide a basis for improved seismic hazard

879   assessments. Additionally, as we are addressing offshore faults exhibiting vertical

880   displacement, our findings can be used to establish the tsunamigenic potential of

881   this region. Furthermore, this approach for incorporating mechanical

882   heterogeneities in the seismogenic crust can be applied to other regions and

883   tectonic settings with analogous structural configurations.

884

885

10. Author contribution

Martin-Rojas, I.: Conceptualization, Data curation, Formal analysis, Funding acquisition, Investigation, Methodology, Project administration, Supervision, Validation, Visualization, Writing – original draft preparation, review & editing

Ramos, A.; Data curation, Formal analysis, Funding acquisition, Investigation, Resources, Visualization, Writing – original draft preparation, review & editing

De Ruig, M.: Data curation, Formal analysis, Investigation, Resources, Visualization, Writing – original draft preparation, review & editing

Medina-Cascales, I.: Data curation, Formal analysis, Investigation, Visualization, Writing –review & editing

Santamaría-Pérez, E.: Data curation, Formal analysis, Investigation, Writing – review & editing

Alfaro, P.: Data curation, Formal analysis, Investigation, Supervision, Writing – review & editing

11. Competing interests

The authors declare that they have no conflict of interest.

13. Financial support

This research was funded by the Spanish Ministry of Science, Innovation and University (research projects PID2021-127967NB-I00 and RTI2018-100737-B-I00), Generalitat Valenciana (Valencian Regional Government, research projects AICO2021/196 and CIAPOS/2022/082, and University of Alicante (research project VIGROB053). The authors acknowledge the use of the MOVE Software Suite granted by PE Limited (Petex).

912   References

913   Agustí, J., Santos-Cubedo, A., Furió, M., De Marfá, R., Blain, H., Oms, O., & Sevilla, P.

914   (2011). The late Neogene-early Quaternary small vertebrate succession from the

915   Almenara-Casablanca karst complex (Castellón, Eastern Spain): Chronologic and

916   paleoclimatic context. *Quaternary International, 243*(1), 183–191.

917   10.1016/j.quaint.2010.11.016

918   Albarracín, S., Alcántara-Carrió, J., Barranco, A., Sánchez García, M. J., Fontán Bouzas, Á,

919   & Rey Salgado, J. (2013). Seismic evidence for the preservation of several stacked

920   Pleistocene coastal barrier/lagoon systems on the Gulf of Valencia continental shelf

921   (western Mediterranean). *Geo-Marine Letters, 33*(2-3), 217–223. 10.1007/s00367-

922   012-0315-x

923   Arche, A., & López-Gómez, J. (1996). Origin of the Permian-Triassic Iberian Basin, central-

924   eastern Spain. *Tectonophysics, 266*(1), 443–464. 10.1016/S0040-1951(96)00202-8

925   Buforn, E., & Udías, A. (2021). *El terremoto de Alcoy de 1620 y la serie sísmica de 1644 en*

926   *la comarca de Muro*. Centro Nacional de Información Geográfica.

927   Buforn, E., Udías, A., Sanz de Galdeano, C., & Cesca, S. (2015). The 1748 Montesa

928   (southeast Spain) earthquake — A singular event. *Tectonophysics, 664*, 139–153.

929   10.1016/j.tecto.2015.09.005

930   Cameselle, A. L., Urgeles, R., De Mol, B., Camerlenghi, A., & Canning, J. C. (2014). Late

931   Miocene sedimentary architecture of the Ebro Continental Margin (Western

932   Mediterranean): implications to the Messinian Salinity Crisis. *International Journal of*

933   *Earth Sciences : Geologische Rundschau, 103*(2), 423–440. 10.1007/s00531-013-

934   0966-5

935 Casciello, E., Vergés, J., Saura, E., Casini, G., Fernández, N., Blanc, E., Homke, S., & Hunt,

936   D. W. (2009). Fold patterns and multilayer rheology of the Lurestan Province, Zagros

937   simply folded belt (Iran). *Journal of the Geological Society, 166*(5), 947–959.

938   10.1144/0016-76492008-138

939 Cheng Jia, C. J., Rong, Y., Magistrale, H., Chen Guihua, C. G., & Xu Xiwei, X. X. (2019a).

940   Earthquake rupture scaling relations for mainland China. *Seismological Research*

941   *Letters, 91*(1), 248–261. 10.1785/0220190129

942 Cheng Jia, C. J., Rong, Y., Magistrale, H., Chen Guihua, C. G., & Xu Xiwei, X. X. (2019b).

943   Earthquake rupture scaling relations for mainland China. *Seismological Research*

944   *Letters, 91*(1), 248–261. 10.1785/0220190129

945 Clavell, E., & Berastegui, X. (1991). Petroleum geology of the Gulf of Valencia. *Generation,*

946   *Accumulation, and Production of Europe's Hydrocarbons,* , 355–368.

947   https://www.scopus.com/inward/record.uri?eid=2-s2.0-

948   0026310072&partnerID=40&md5=8f34c3d495738519a9101eb775a91bd4

949 De Ruig, & M.J. (1992). *Tectono-sedimentary evolution of the Prebetic fold belt of Alicante*

950 Del Rio, V. D., Rey, J., & Vegas, R. (1986). The Gulf of Valencia continental shelf:

951   Extensional tectonics in Neogene and Quaternary sediments. *Marine Geology, 73*(1),

952   169–179. 10.1016/0025-3227(86)90117-9

953 DeMets, C., Gordon, R. G., Argus, D. F., & Stein, S. (1994). Effect of recent revisions to the

954   geomagnetic reversal time scale on estimates of current plate motions. *Geophysical*

955   *Research Letters, 21*(20), 2191–2194. 10.1029/94GL02118

956   Duffy, O. B., Gawthorpe, R. L., & Docherty, M. (2023). Tectono-stratigraphic evolution of

957   salt-influenced normal fault systems: an example from the Coffee-Soil Fault, Danish

958   North Sea. *Journal of the Geological Society, 180*(6), 1. 10.1144/jgs2023-016

959   Etheve, N., Frizon de Lamotte, D., Mohn, G., Martos, R., Roca, E., & Blanpied, C. (2016).

960   Extensional vs contractional Cenozoic deformation in Ibiza (Balearic Promontory,

961   Spain): Integration in the West Mediterranean back-arc setting. *Tectonophysics, 682*,

962   35–55. 10.1016/j.tecto.2016.05.037

963   Faccenna, C., Piromallo, C., Crespo-Blanc, A., Jolivet, L., & Rossetti, F. (2004a). Lateral

964   slab deformation and the origin of the western Mediterranean arcs. *Tectonics

965   (Washington, D.C.), 23*(1), np–n/a. 10.1029/2002TC001488

966   Faccenna, C., Piromallo, C., Crespo-Blanc, A., Jolivet, L., & Rossetti, F. (2004b). Lateral

967   slab deformation and the origin of the western Mediterranean arcs. *Tectonics

968   (Washington, D.C.), 23*(1), np–n/a. 10.1029/2002TC001488

969   Fang, P., Tugend, J., Mohn, G., Kusznir, N., & Ding, W. (2021a). Evidence for rapid large-

970   amplitude vertical motions in the Valencia Trough (Western Mediterranean)

971   generated by 3D subduction slab roll-back. *Earth and Planetary Science Letters, 575*,

972   117179. 10.1016/j.epsl.2021.117179

973   Fang, P., Tugend, J., Mohn, G., Kusznir, N., & Ding, W. (2021b). Evidence for rapid large-

974   amplitude vertical motions in the Valencia Trough (Western Mediterranean)

975   generated by 3D subduction slab roll-back. *Earth and Planetary Science Letters, 575*,

976   117179. 10.1016/j.epsl.2021.117179

977   Ford, M., Le Carlier de Veslud, C., & Bourgeois, O. (2007). Kinematic and geometric

978   analysis of fault-related folds in a rift setting: The Dannemarie basin, Upper Rhine

979   Graben, France. *Journal of Structural Geology, 29*(11), 1811–1830.

980   10.1016/j.jsg.2007.08.001

981   García-Mayordomo, J., Insua-Arévalo, J. M., Martínez-Díaz, J. J., Jiménez-Díaz, A., Martín-

982   Banda, R., Martín-Alfageme, S., Álvarez-Gómez, J. A., Rodríguez-Peces, M., Pérez-

983   López, R., Rodríguez-Pascua, M. A., Masana, E., Perea, H., Martín-González, F.,

984   Giner-Robles, J., Nemser, E. S., & Cabral, J. (2012). The Quaternary active faults

985   database of Iberia (QAFI v. 2.0). *Journal of Iberian Geology,*

986   *38*(1)10.5209/rev_JIGE.2012.v38.n1.39219

987   Gaspar-Escribano, J. M., Garcia-Castellanos, D., Roca, E., & Cloetingh, S. (2004).

988   Cenozoic vertical motions of the Catalan Coastal Ranges (NE Spain): The role of

989   tectonics, isostasy, and surface transport. *Tectonics (Washington, D.C.), 23*(1), np–

990   n/a. 10.1029/2003TC001511

991   Geel, T. (1995). Oligocene to early Miocene tectono-sedimentary history of the Alicante

992   region (SE Spain): implications for Western Mediterranean evolution. *Basin Research,*

993   *7*(4), 313–336. 10.1111/j.1365-2117.1995.tb00120.x

994   Geller, R. J. (1976). Scaling relations for earthquake source parameters and magnitudes.

995   *Bulletin of the Seismological Society of America, 66*(5), 1501–1523.

996   https://pubs.geoscienceworld.org/ssa/bssa/article/66/5/1501/117604

997   González, Á. (2017). The Spanish National Earthquake Catalogue: Evolution, precision and

998   completeness. *Journal of Seismology, 21*(3), 435–471. 10.1007/s10950-016-9610-8

999   Guimera, J., & Alvaro, M. (1990). Structure et évolution de la compression alpine dans la

1000   Chaîne ibérique et la Chaîne côtière catalane (Espagne). *Bulletin De La Société*

1001   *Géologique De France, 6*(2), 339–348. 10.2113/gssgfbull.VI.2.339

1002   Hongxing, G., & Anderson, J. K. (2007). Fault throw profile and kinematics of Normal fault:

1003   conceptual models and geologic examples. *Geological Journal of China Universities,*

1004   *13*(1), 75.

1005   Huang, J., Abrahamson, N. A., Sung, C., & Chao, S. (2024). New Empirical Source-Scaling

1006   Laws for Crustal Earthquakes Incorporating Fault Dip and Seismogenic-Thickness

1007   Effects. *Seismological Research Letters, 95*(4), 2352–2367. 10.1785/0220240034

1008   Hyndman, R. D., Yamano, M., & Oleskevich, D. A. (1997). The seismogenic zone of

1009   subduction thrust faults. *Island Arc, 6*(3), 244–260. 10.1111/j.1440-

1010   1738.1997.tb00175.x

1011   IGN. (2025). *Instituto Geográfico Nacional (2025) Servicio de Información Sísmica.*

1012   Jackson, C. A. -., & Rotevatn, A. (2013). 3D seismic analysis of the structure and evolution

1013   of a salt-influenced normal fault zone: A test of competing fault growth models.

1014   *Journal of Structural Geology, 54*, 215–234. 10.1016/j.jsg.2013.06.012

1015   Jackson, M. P. A., & Hudec, M. R. (2005). Stratigraphic record of translation down ramps in

1016   a passive-margin salt detachment. *Journal of Structural Geology, 27*(5), 889–911.

1017   10.1016/j.jsg.2005.01.010

1018   Jolivet, L., & Faccenna, C. (2000). Mediterranean extension and the Africa-Eurasia

1019   collision. *Tectonics, 19*(6), 1095–1106. 10.1029/2000TC900018

1020   Kanamori, H., & Anderson, D. L. (1975). Theoretical basis of some empirical relations in

1021   seismology. *Bulletin of the Seismological Society of America, 65*(5), 1073–1095.

1022   https://pubs.geoscienceworld.org/ssa/bssa/article/65/5/1073/117458

1023   Kane, K. E., Jackson, C. A. -., & Larsen, E. (2010). Normal fault growth and fault-related

1024   folding in a salt-influenced rift basin: South Viking Graben, offshore Norway. *Journal*

1025   *of Structural Geology, 32*(4), 490–506. 10.1016/j.jsg.2010.02.005

1026   Leonard, M. (2010). Earthquake fault scaling; self-consistent relating of rupture length,

1027   width, average displacement, and moment release. *Bulletin of the Seismological*

1028   *Society of America, 100*(5A), 1971–1988. 10.1785/0120090189

1029   Leonard, M. (2014). Self-consistent earthquake fault-scaling relations; update and

1030   extension to stable continental strike-slip faults. *Bulletin of the Seismological Society*

1031   *of America, 104*(6), 2953–2965. 10.1785/0120140087

1032   Lirer, F., Foresi, L. M., Iaccarino, S. M., Salvatorini, G., Turco, E., Cosentino, C., Sierro, F.

1033   J., & Caruso, A. (2019). Mediterranean Neogene planktonic foraminifer biozonation

1034   and biochronology. *Earth-Science Reviews, 196*, 102869.

1035   10.1016/j.earscirev.2019.05.013

1036   Lofi, J. (2011). *Seismic atlas of the "Messinian salinity crisis" markers in the Mediterranean*

1037   *and Black Seas*. Commission for the Geological Map of the World.

1038   Maillard, A., Mauffret, A., Watts, A. B., Torné, M., Pascal, G., Buhl, P., & Pinet, B. (1992).

1039   Tertiary sedimentary history and structure of the Valencia trough (western

1040   Mediterranean). *Tectonophysics, 203*(1), 57–75. 10.1016/0040-1951(92)90215-R

1041   Maillard, A., & Mauffret, A. (2013). Structure and present-day compression in the offshore

1042   area between Alicante and Ibiza Island (Eastern Iberian Margin). *Tectonophysics,*

1043   *591*, 116–130. 10.1016/j.tecto.2011.07.007

1044   Mansfield, C. S., & Cartwright, J. A. (1996). High resolution fault displacement mapping

1045   from three-dimensional seismic data: evidence for dip linkage during fault growth.

1046   *Journal of Structural Geology, 18*(2), 249–263. 10.1016/S0191-8141(96)80048-4

1047   Marsh, N., Imber, J., Holdsworth, R. E., Brockbank, P., & Ringrose, P. (2010). The structural

1048   evolution of the Halten Terrace, offshore Mid-Norway: extensional fault growth and

1049   strain localisation in a multi-layer brittle-ductile system. *Basin Research, 22*(2), 195–

1050   214. 10.1111/j.1365-2117.2009.00404.x

1051   Martí, J., Mitjavila, J., Roca, E., & Aparicio, A. (1992). Cenozoic magmatism of the valencia

1052   trough (western mediterranean): Relationship between structural evolution and

1053   volcanism. *Tectonophysics, 203*(1), 145–165. 10.1016/0040-1951(92)90221-Q

1054   Martínez-Solares, J. M., & Mezcua, J. (2002). *Catálogo sísmico de la Península Ibérica*.

1055   Madrid (Spain): Instituto Geográfico Nacional.

1056   Maurin, J., & Niviere, B. (1999). Extensional forced folding and décollement of the pre-rift

1057   series along the Rhine graben and their influence on the geometry of the syn-rift

1058   sequences. *Forced Folds and Fractures* (pp. 73–86). The Geological Society of

1059   London. 10.1144/GSL.SP.2000.169.01.06

1060   McClusky, S., Reilinger, R., Mahmoud, S., Ben Sari, D., & Tealeb, A. (2003). GPS

1061   constraints on Africa (Nubia) and Arabia plate motions. *Geophysical Journal

1062   International, 155*(1), 126–138. 10.1046/j.1365-246X.2003.02023.x

1063   Molinaro, M., Leturmy, P., Guezou, J. -., Frizon de Lamotte, D., & Eshraghi, S. A. (2005).

1064   The structure and kinematics of the southeastern Zagros fold-thrust belt, Iran: From

1065   thin-skinned to thick-skinned tectonics. *Tectonics, 24*(3), np–n/a.

1066   10.1029/2004TC001633

1067   Morley, C. K., Back, S., Van Rensbergen, P., Crevello, P., & Lambiase, J. J. (2003).

1068   Characteristics of repeated, detached, Miocene–Pliocene tectonic inversion events,

1069   in a large delta province on an active margin, Brunei Darussalam, Borneo. *Journal of*

1070   *Structural Geology, 25*(7), 1147–1169. 10.1016/S0191-8141(02)00130-X

1071   NEBOT, M., & GUIMERÀ, J. (2018). Kinematic evolution of a fold-and-thrust belt developed

1072   during basin inversion: the Mesozoic Maestrat basin, E Iberian Chain. *Geological*

1073   *Magazine, 155*(3), 630–640. 10.1017/S001675681600090X

1074   Nicol, A., Watterson, J., Walsh, J. J., & Childs, C. (1996). The shapes, major axis

1075   orientations and displacement patterns of fault surfaces. *Journal of Structural*

1076   *Geology, 18*(2), 235–248. 10.1016/S0191-8141(96)80047-2

1077   Nissen, E., Ghorashi, M., Jackson, J., Parsons, B., & Talebian, M. (2007). The 2005 Qeshm

1078   Island earthquake (Iran)—a link between buried reverse faulting and surface folding

1079   in the Zagros Simply Folded Belt? *Geophysical Journal International, 171*(1), 326–338.

1080   10.1111/j.1365-246X.2007.03514.x

1081   Nissen, E., Tatar, M., Jackson, J. A., & Allen, M. B. (2011). New views on earthquake

1082   faulting in the Zagros fold-and-thrust belt of Iran. *Geophysical Journal International,*

1083   *186*(3), 928–944. 10.1111/j.1365-246X.2011.05119.x

1084   Nocquet, J. -., & Calais, E. (2003). Crustal velocity field of western Europe from permanent

1085   GPS array solutions, 1996–2001. *Geophysical Journal International, 154*(1), 72–88.

1086   10.1046/j.1365-246X.2003.01935.x

1087   Nocquet, J. (2012). Present-day kinematics of the Mediterranean: A comprehensive

1088   overview of GPS results. *Tectonophysics, 579*, 220–242. 10.1016/j.tecto.2012.03.037

1089   Palano, M., González, P. J., & Fernández, J. (2015). The Diffuse Plate boundary of Nubia

1090   and Iberia in the Western Mediterranean: Crustal deformation evidence for viscous

1091   coupling and fragmented lithosphere. *Earth and Planetary Science Letters, 430*, 439–

1092   447. 10.1016/j.epsl.2015.08.040

1093   Pascal, G., Torné, M., Buhl, P., Watts, A. B., & Mauffret, A. (1992). Crustal and velocity

1094   structure of the Valencia trough (western Mediterranean), Part II. Detailed

1095   interpretation of five Expanded Spread Profiles. *Tectonophysics, 203*(1), 21–35.

1096   10.1016/0040-1951(92)90213-P

1097   PASCOE, R., HOOPER, R., STORHAUG, K., & HARPER, H. (Jan 1, 1999). Evolution of

1098   extensional styles at the southern termination of the Nordland Ridge, Mid-Norway: a

1099   response to variations in coupling above Triassic salt. Paper presented at the *, 5*(1)

1100   83–90. 10.1144/0050083 https://www.lyellcollection.org/doi/10.1144/0050083

1101   Perea, H. (2006). *Falles actives i perillositat sísmica al marge nord-occidental del solc de*

1102   *València*

1103   Pérez-Peña, A., Martín-Davila, J., Gárate, J., Berrocoso, M., & Buforn, E. (2010). Velocity

1104   field and tectonic strain in Southern Spain and surrounding areas derived from GPS

1105   episodic measurements. *Journal of Geodynamics, 49*(3), 232–240.

1106   10.1016/j.jog.2010.01.015

1107   Ramos, A., Lopez-Mir, B., Wilson, E. P., Granado, P., & Muñoz, J. A. (2020). 3D

1108   reconstruction of syn-tectonic strata in a salt-related orogen: learnings from the Llert

1109   syncline (South-central Pyrenees). *Acta Geologica Hispanica, 18*(1), 1–19.

1110   10.1344/GeologicaActa2020.18.20

1111   Ramos, A., de Ruig, M. J., Pedrera, A., Alfaro, P., & Martin-Rojas, I. (2025). Salt expulsion

1112   triggered by prograding clinoforms in the SW Valencia Trough (SE Spain). *Marine and*

1113   *Petroleum Geology, 173*, 107268. 10.1016/j.marpetgeo.2024.107268

1114   Ramos, A., Pedrera, A., García-Senz, J., López-Mir, B., & Salas, R. (2023). Seismic

1115   evidence for ductile necking of the mid-lower crust beneath the Columbrets Basin

1116   (Western Mediterranean). *Terra Nova (Oxford, England), 35*(5), 404–412.

1117   10.1111/ter.12664

1118   Rehault, J., Boillot, G., & Mauffret, A. (1984). The Western Mediterranean Basin geological

1119   evolution. *Marine Geology, 55*(3), 447–477. 10.1016/0025-3227(84)90081-1

1120   Ribó, M., Puig, P., Muñoz, A., Lo Iacono, C., Masqué, P., Palanques, A., Acosta, J., Guillén,

1121   J., & Gómez Ballesteros, M. (2016a). Morphobathymetric analysis of the large fine-

1122   grained sediment waves over the Gulf of Valencia continental slope (NW

1123   Mediterranean). *Geomorphology, 253*, 22–37. 10.1016/j.geomorph.2015.09.027

1124   Ribó, M., Puig, P., Urgeles, R., Van Rooij, D., & Muñoz, A. (2016b). Spatio-temporal

1125   evolution of sediment waves developed on the Gulf of Valencia margin (NW

1126   Mediterranean) during the Plio-Quaternary. *Marine Geology, 378*, 276–291.

1127   10.1016/j.margeo.2015.11.011

1128   Richardson, N. J., Underhill, J. R., & Lewis, G. (2005). The role of evaporite mobility in

1129   modifying subsidence patterns during normal fault growth and linkage, Halten

1130   Terrace, Mid-Norway. *Basin Research, 17*(2), 203–223. 10.1111/j.1365-

1131   2117.2005.00250.x

1132   Roca, E. (1994). La evolución geodinámica de la Cuenca Catalano-Balear y áreas

1133   adyacentes desde el Mesozoico hasta la actualidad. *Acta Geologica Hispanica,*

1134   *29*(1), 3–25. https://raco.cat/index.php/ActaGeologica/article/view/75462

1135   Roca, E. (2001). The Northwest Mediterranean Basin (Valencia Trough, Gulf of Lions and

1136   Liguro-Provencal basins): structure and geodynamic evolution. *Mem. Mus. Natl. Hist.*

1137   *Nat. (France)* (pp. 671–706)

1138   Roca, E., Frizon de Lamotte, D., Mauffret, A., Bracene, R., Verges, J., Benaouali, N.,

1139   Fernandez, M., Munoz, J. A., & Zeyen, H. (2004). TRANSMED-transect II (Aquitaine

1140   basin, Pyrenees, Ebro basin, Catalan coastal ranges, Valancia trough, Balearic

1141   promontory, Algerian basin, Tell, Sahara Atlas, Sahara platform). In : W. Cavazza, F.

1142   Roure, W. Spakman, G.M. Stampfli and P.A. Ziegler (Eds). The TRANSMED Atlas - the

1143   Mediterranean region from Crust to Mantle. *Springer, Berlin* https://hal.science/hal-

1144   00069583

1145   Roca, E., & Desegaulx, P. (1992). Analysis of the geological evolution and vertical

1146   movements in the València Trough area, western Mediterranean. *Marine and*

1147   *Petroleum Geology, 9*(2), 167,IN1,177–176,IN8,185. 10.1016/0264-8172(92)90089-W

1148   Roca, E., & Guimerà, J. (1992). The Neogene structure of the eastern Iberian margin:

1149   Structural constraints on the crustal evolution of the Valencia trough (western

1150   Mediterranean). *Tectonophysics, 203*(1), 203–218. 10.1016/0040-1951(92)90224-T

1151   Roca, E., Sans, M., Cabrera, L., & Marzo, M. (1999). Oligocene to Middle Miocene

1152   evolution of the central Catalan margin (northwestern Mediterranean).

1153   *Tectonophysics, 315*(1), 209–229. 10.1016/S0040-1951(99)00289-9

1154   Rouby, D., Guillocheau, F., Robin, C., Bouroullec, R., Raillard, S., Castelltort, S., & Nalpas,

1155   T. (2003). Rates of deformation of an extensional growth fault/raft system (offshore

1156   Congo, West African margin) from combined accommodation measurements and 3-

1157   D restoration. *Basin Research, 15*(2), 183–200. 10.1046/j.1365-2117.2003.00200.x

1158   Roustaei, M., Nissen, E., Abbassi, M., Gholamzadeh, A., Ghorashi, M., Tatar, M., Yamini-

1159   Fard, F., Bergman, E., Jackson, J., & Parsons, B. (2010). The 2006 March 25 Fin

1160   earthquakes (Iran)—insights into the vertical extents of faulting in the Zagros Simply

1161   Folded Belt. *Geophysical Journal International, 181*(3), 1275–1291. 10.1111/j.1365-

1162   246X.2010.04601.x

1163   Ruff, L., & Kanamori, H. (1983). Seismic coupling and uncoupling at subduction zones.

1164   *Tectonophysics, 99*(2), 99–117. 10.1016/0040-1951(83)90097-5

1165   Ruig, M. J. d. (1996). Extensional diapirism in the eastern Prebetic foldbelt, southeastern

1166   Spain. *AAPG Memoir,* (65) https://www.osti.gov/biblio/585188

1167   Sàbat, F., Gelabert, B., Rodríguez-Perea, A., & Giménez, J. (2011). Geological structure

1168   and evolution of Majorca: Implications for the origin of the Western Mediterranean.

1169   *Tectonophysics, 510*(1), 217–238. 10.1016/j.tecto.2011.07.005

1170   SALAS, R., GUIMERA, J., MAS, R., MARTIN-CLOSAS, C., MELENDEZ, A., & ALONSO, A.

1171   (2001a). Evolution of the Mesozoic Central Iberian Rift System and its Cainozoic

1172   inversion (Iberian chain). *Mémoires Du Muséum National D'histoire Naturelle (1993),*

1173   *186*, 145–186.

1174   SALAS, R., GUIMERA, J., MAS, R., MARTIN-CLOSAS, C., MELENDEZ, A., & ALONSO, A.

1175   (2001b). Evolution of the Mesozoic Central Iberian Rift System and its Cainozoic

1176   inversion (Iberian chain). *Mémoires Du Muséum National D'histoire Naturelle (1993),*

1177   *186*, 145–186.

1178   Seranne, M. (1999). The Gulf of Lion continental margin (NW Mediterranean) revisited by

1179   IBS: an overview. *Geological Society special publication* (pp. 15–36). The Geological

1180   Society of London. 10.1144/GSL.SP.1999.156.01.03

1181   Serpelloni, E., Vannucci, G., Pondrelli, S., Argnani, A., Casula, G., Anzidei, M., Baldi, P., &

1182   Gasperini, P. (2007). Kinematics of the Western Africa-Eurasia plate boundary from

1183   focal mechanisms and GPS data. *Geophysical Journal International, 169*(3), 1180–

1184   1200. 10.1111/j.1365-246X.2007.03367.x

1185   Sherkati, S., Molinaro, M., Frizon de Lamotte, D., & Letouzey, J. (2005). Detachment

1186   folding in the Central and Eastern Zagros fold-belt (Iran): salt mobility, multiple

1187   detachments and late basement control. *Journal of Structural Geology, 27*(9), 1680–

1188   1696. 10.1016/j.jsg.2005.05.010

1189   Soler y José, R., Martínez del Olmo, W., Megías, A. G., & Abeger Monteagudo, J. A. (1983).

1190   Rasgos básicos del neógeno del Mediterráneo español. *Mediterránea. Serie de*

1191   *Estudios Geológicos, 1*, 71–82.

1192   STAMPFLI, G. M., & HOCKER, C. F. W. (1989). Messinian palaeorelief from a 3-D seismic

1193   survey in the Tarraco concession area (Spanish Mediterranean Sea). *Geologie En*

1194   *Mijnbouw, 68*(2), 201–210.

1195   Stewart, S. A., Ruffell, A. H., & Harvey, M. J. (1997). Relationship between basement-linked

1196   and gravity-driven fault systems in the UKCS salt basins. *Marine and Petroleum*

1197   *Geology, 14*(5), 581–604. 10.1016/S0264-8172(97)00008-1

1198   Stich, D., Martín, R., & Morales, J. (2010). *Moment tensor inversion for Iberia-Maghreb*

1199   *earthquakes 2005-2008*. Elsevier.

1200   Stich, D., Serpelloni, E., de Lis Mancilla, F., & Morales, J. (2006). Kinematics of the Iberia–

1201   Maghreb plate contact from seismic moment tensors and GPS observations.

1202   *Tectonophysics, 426*(3), 295–317. 10.1016/j.tecto.2006.08.004

1203   Stirling, M., Goded, T., Berryman, K., & Litchfield, N. (2013). Selection of earthquake

1204   scaling relationships for seismic-hazard analysis. *Bulletin of the Seismological*

1205   *Society of America, 103*(6), 2993–3011. 10.1785/0120130052

1206   Stirling, M., Rhoades, D., & Berryman, K. (2002). Comparison of earthquake scaling

1207   relations derived from data of the instrumental and preinstrumental era. *Bulletin of*

1208   *the Seismological Society of America, 92*(2), 812–830. 10.1785/0120000221

1209   Stock, C., & Smith, E. G. C. (2000). Evidence for different scaling of earthquake source

1210   parameters for large earthquakes depending on faulting mechanism. *Geophysical*

1211   *Journal International, 143*(1), 157–162. 10.1046/j.1365-246x.2000.00225.x

1212   Thorsen, C. E. (1963). Age of growth faulting in southeast Louisiana.

1213   Torné, M., Pascal, G., Buhl, P., Watts, A. B., & Mauffret, A. (1992). Crustal and velocity

1214   structure of the Valencia trough (western Mediterranean), Part I. A combined

1215   refraction/ wide-angle reflection and near-vertical reflection study. *Tectonophysics,*

1216   *203*(1), 1–20. 10.1016/0040-1951(92)90212-O

1217   Tvedt, A. B. M., Rotevatn, A., Jackson, C. A. -., Fossen, H., & Gawthorpe, R. L. (2013).

1218   Growth of normal faults in multilayer sequences: A 3D seismic case study from the

1219 Egersund Basin, Norwegian North Sea. *Journal of Structural Geology, 55*, 1–20.

1220 10.1016/j.jsg.2013.08.002

1221 van Hinsbergen, D. J. J., Torsvik, T. H., Schmid, S. M., Maţenco, L. C., Maffione, M.,

1222 Vissers, R. L. M., Gürer, D., & Spakman, W. (2020). Orogenic architecture of the

1223 Mediterranean region and kinematic reconstruction of its tectonic evolution since the

1224 Triassic. *Gondwana Research, 81*, 79–229. 10.1016/j.gr.2019.07.009

1225 van Hinsbergen, D. J. J., Vissers, R. L. M., & Spakman, W. (2014). Origin and consequences

1226 of western Mediterranean subduction, rollback, and slab segmentation. *Tectonics*

1227 *(Washington, D.C.), 33*(4), 393–419. 10.1002/2013TC003349

1228 Vargas, H., Gaspar-Escribano, J. M., López-Gómez, J., Van Wees, J., Cloetingh, S., de La

1229 Horra, R., & Arche, A. (2009). A comparison of the Iberian and Ebro Basins during the

1230 Permian and Triassic, eastern Spain: A quantitative subsidence modelling approach.

1231 *Tectonophysics, 474*(1), 160–183. 10.1016/j.tecto.2008.06.005

1232 Verges, J., & Sabat, F. (1999). Constraints on the Neogene Mediterranean kinematic

1233 evolution along a 1000 km transect from Iberia to Africa. *Geological Society special*

1234 *publication* (pp. 63–80). The Geological Society of London.

1235 10.1144/GSL.SP.1999.156.01.05

1236 Verges, J., & Fernandez, M. (2012). Tethys–Atlantic interaction along the Iberia–Africa

1237 plate boundary: The Betic–Rif orogenic system. *Tectonophysics, 579*, 144–172.

1238 10.1016/j.tecto.2012.08.032

1239 Wells, D. L., & Coppersmith, K. J. (1994). New empirical relationships among magnitude,

1240 rupture length, rupture width, rupture area, and surface displacement. *Bulletin of the*

1241   *Seismological Society of America, 84*(4), 974–1002.

1242   https://pubs.geoscienceworld.org/ssa/bssa/article/84/4/974/119792

1243   Weng, H., & Yang, H. (2017). Seismogenic width controls aspect ratios of earthquake

1244   ruptures. *Geophysical Research Letters, 44*(6), 2725–2732. 10.1002/2016gl072168

1245   Withjack, M. O., & Callaway, S. (2000). Active normal faulting beneath a salt layer; an

1246   experimental study of deformation patterns in the cover sequence. *AAPG Bulletin,*

1247   *84*(5), 627–651. 10.1306/C9EBCE73-1735-11D7-8645000102C1865D

1248   Withjack, M. O., Olson, J., & Peterson, E. (1990). Experimental models of extensional

1249   forced folds. *AAPG Bulletin, 74*(7), 1038–1054. 10.1306/0C9B23FD-1710-11D7-

1250   8645000102C1865D

1251   Yen, Y., & Ma, K. (2011a). Source-scaling relationship for M 4.6-8.9 earthquakes,

1252   specifically for earthquakes in the collision zone of Taiwan. *Bulletin of the*

1253   *Seismological Society of America, 101*(2), 464–481. 10.1785/0120100046

1254   Yen, Y., & Ma, K. (2011b). Source-scaling relationship for M 4.6-8.9 earthquakes,

1255   specifically for earthquakes in the collision zone of Taiwan. *Bulletin of the*

1256   *Seismological Society of America, 101*(2), 464–481. 10.1785/0120100046

1257   Zazo, C. (1979). El problema del límite Plio-Pleistoceno en el litoral S y SE de España.

1258   *Trabajos N/Q, 9*, 65–72.

1259

1260

1261